Visual analysis of hydrate growth and layering behaviour in hydrate bearing silica and quartz sediments

Jan Erik Kaarhus Parkinson

Master's thesis in Reservoir Chemistry

Department of Chemistry – University of Bergen

June 2020

Supervisor: Tanja Barth

Abstract

Gas hydrates are crystalline solids with cage-like structures of water containing a guest molecule. They have sparked great interest due to their potential as an energy source, and the possibility of utilizing them for carbon capture and storage. In the North Sea, natural gas hydrates are found dispersed in fine grained sediments. Most previous laboratory studies on hydrates in sediments have focused on formation in coarse-grained sediments and intrapore hydrate behaviour (1) (2). More research is therefore required on hydrate formation behaviour fine-grained sediments.

This thesis presents a study on macroscopic hydrate formation behaviour in colloidal silica and fine-grained quartz sediments. Tetrahydrofuran (THF) is used as hydrate former in place of methane, as it forms hydrates at atmospheric pressure. The formation of hydrates is recorded by a camera over a span of 24 to 48 hours, and colouring is used to enhance visibility. A range of experiments are set up to observe hydrate growth within varying environmental conditions, such as electrolyte content and porosity. Magnetic resonance imaging (MRI) is also used to observe hydrate formation behaviour from within samples.

Hydrates were observed to form nodes, veins, channels and layers in colloidal silica and fine-grained quartz sediments. The formation behaviour was seen to depend on reaction kinetics. Slow hydrate formation saw the build-up of larger hydrate crystals, while fast hydrate growth saw a fine dispersion of hydrates with less tendency to displace sediments. Colloidal suspensions saw a more complete and dispersed hydrate growth, while larger but fewer hydrate structures were observed in the more dense sediments. Utsira formation water with an electrolyte content of roughly 3,2 weight percent was also seen to greatly enhance hydrate growth, despite its salt content.

Due to the COVID-19 pandemic, planned experiments using Equinor's MRI instrument had to be cancelled. Only a few images were therefore extracted. These images provide the methodology for the MRI experiments, and provide evidence that hydrate layering behaviour is also prevalent within the undisturbed sediments.

Acknowledgements

First, I would like to express my gratitude to my supervisor Tanja Barth at the Department of Chemistry at the University of Bergen. Your ideas and excellent guidance are what made this thesis on gas hydrates possible. I am grateful that you took time out of your schedule to help whenever needed. Your support and encouragement are sources of great motivation.

I would also like to thank Per Fotland for providing me the opportunity to perform MRI studies at Equinor Sandsli. Furthermore, I would like to thank Gry Lien Aastveit from Equinor. Her contributions to the MRI studies have also been invaluable.

Finally, I would like to thank my friends and family, and most importantly my dearest Hanne Stiegler Larsen. Not only have you supported me throughout my entire studies, but also continuously motivated me throughout the hardships of a global pandemic. I am lucky to have you by my side.

Bergen - June 2020

Jan Erik Parkinson

Table of contents

1 Introduction

1.1 Clathrate Hydrates

Clathrate hydrates are non-stoichiometric crystalline solids consisting of a lattice structure of water, with guest molecules occupying cavities of the host structure. Both the host and guest molecules interact via van der Waals forces or hydrogen bonding. Typical natural gas hydrates include guest molecules like methane, ethane, propane and CO_2.

Hydrates form at low temperatures and high pressures and are prevalent in permafrost regions and marine sediments. They have been known of for roughly 200 years and only more recently became a field of special interest. This is due to both the challenges of pipeline plugging in production and transport in the petroleum industry and gas hydrates' potential as a fuel source and its role in climate change (3).

Figure 1-1: Pipeline plugged by gas hydrates (4) .

1.2 Global estimations of hydrate reserves

Global estimations of hydrate bound gas vary considerably between sources, but it is widely accepted that global gas hydrate reserves far exceed coal, natural gas and oil reserves combined. Between 1990 and 2004 the global estimate of $21*10^{15}m^3$ of methane at STP (10 000 Gt of methane carbon) was proposed as a consensus value from several independent estimations (5). More recent estimates by e.g. the U.S Department of Energy (DOE) and U.S Geological Survey (USGS) suggest that there are about $3*10^{15}$ m^3 (1800 Gt of methane carbon) (6). The global estimates have decreased over time as a result of growing knowledge

of the distribution and concentration of gas hydrates in marine sediments along with efforts to better constrain the volume of hydrate-bearing sediments and their gas yield (5).

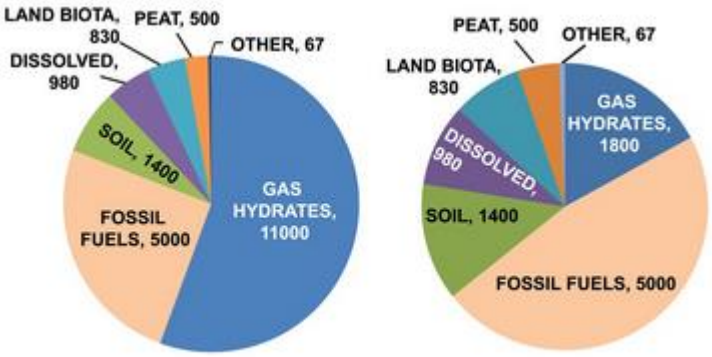

Figure 1-2: The shrinkage of global mobile carbon estimates in gas hydrates over the past few decades. The left chart describes estimates from Kvenvolden [1988] and the right chart shows values close to the estimates by Milkov [2004] and Boswell and Collett [2011] (7)

1.3 Hydrate occurrence in nature

Gas hydrates occur in the gas hydrate stability zone (GHSZ). The upper and lower limits of the GHSZ and its thickness depend on local geological conditions. The low temperatures and high pressures required for gas hydrate formation generally restricts natural deposits to deep oceanic and permafrost regions.

The following diagram displays idealized gas hydrate stability conditions in both a marine setting and in permafrost. Both pressure and temperature increase with depth. The blue solid line denotes the hydrothermal gradient above the seafloor and the geothermal gradient below. The orange solid line denotes the temperature limit at which gas hydrates may form at a given depth/pressure. Hydrates occur in the area between the two curves. The thickness of the GHSZ is typically a few hundred meters. The maximum depth at which hydrates may occur are limited by the geothermal gradient. Kvenvolden (1993) claims a maximum lower GHSZ limit of 2000m, but the limit is typically significantly lower depending on local conditions (8).

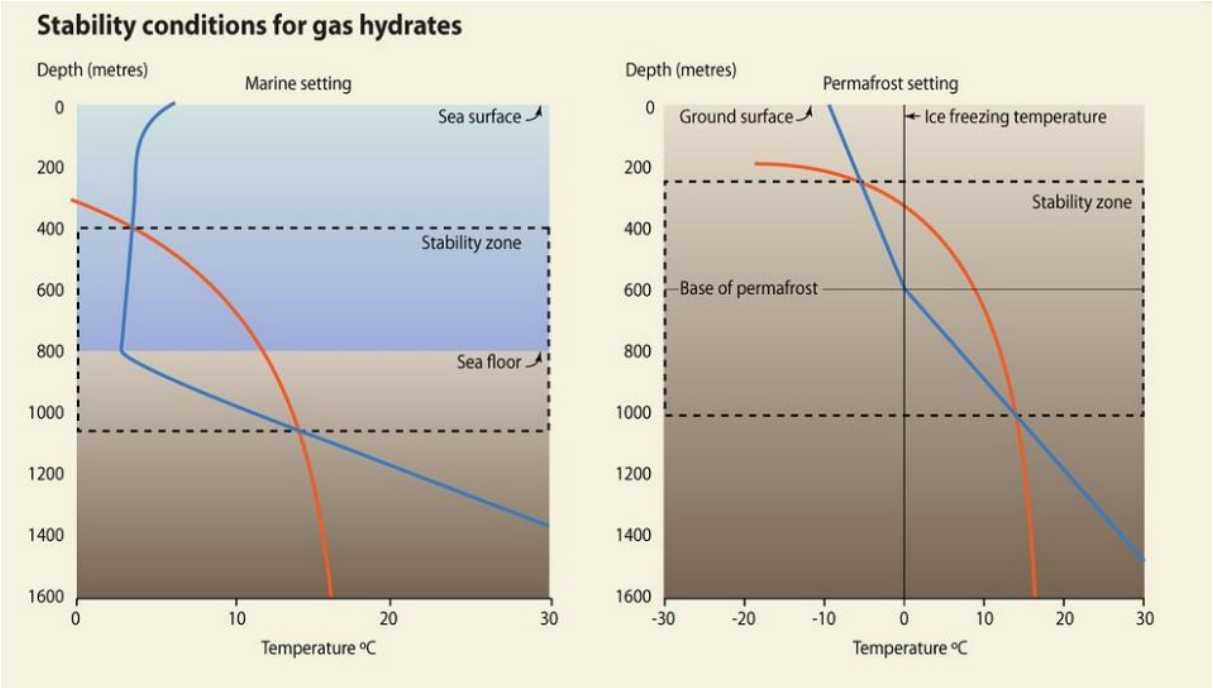

Figure 1-3: Hydrate stability conditions for marine settings (left) and permafrost settings (right) (9). The solid blue line represents the hydrothermal gradient above the seafloor and geothermal gradient below. The Orange line represents the gas hydrate equilibrium line. The dotted area represents the GHSZ.

1.4 Environmental concerns of natural gas hydrates

Permafrost and marine-borne gas hydrates are a sizeable carbon reservoir and an important aspect of the carbon cycle. Concern has grown considerably due to the unstable nature of natural gas hydrates. Both permafrost and marine- associated hydrates are susceptible to dissociation under warming climates, releasing methane into the atmosphere.

Methane is a greenhouse gas whose global warming potential index (GWP) is 20 times that of CO_2 by weight (10). The decomposition of large deposits of methane hydrates may lead to temporary increases in global atmospheric temperatures, which again accelerates the release of methane in a dramatic chain effect.

Another concern is that hydrates directly affect the macroscopic properties of the seafloor. Hydrates formation behaviours include load bearing and cementation of intergranular contacts. Hydrates bridging grains and cementing intergranular contacts contributes significant mechanical stability by becoming a part of the load-bearing framework (11). The dissociation of load bearing hydrates may cause seafloor slope instabilities, increasing the risk of hazards such as submarine landslides.

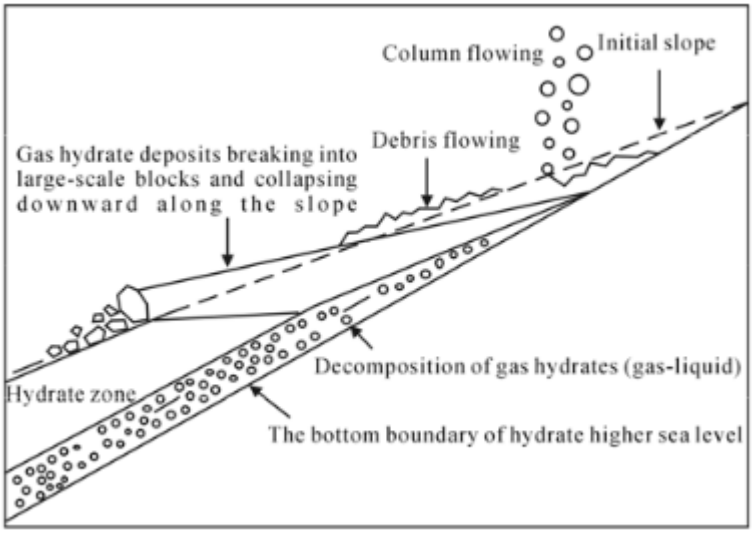

Figure 1-4: Decomposition of load-bearing hydrates leading to submarine landslides (10).

Gas hydrates reservoirs represent a source of carbon sequestration and economic potential. The importance of understanding hydrate formation, morphology and hydrate induced mechanical stability must be emphasized for safe development and environmentally friendly utilization of gas hydrates.

1.5 Structure and physical properties of clathrate hydrates:

The clathrate hydrate host may form lattices of various geometric shapes and sizes. The three most common structures are structure I, II and H. The hydrate structures are composed of five different polyhedral cells formed by hydrogen bonded water molecules. The nomenclature description for polyhedra is n_i^{mi}, where n_i describes the number of edges in the face type "i" and m_i is the amount of faces with n_i *edges.* The pentagonal dodecahedron is labelled 5^{12} because it's has 12 pentagonal faces of equal length and angles. The 16-hedron is labelled $5^{12}6^2$ because it has 12 pentagonal and two hexagonal faces. Each polyhedral unit contains at most a single guest molecule held in place by dispersion forces. The figure below describes the three common clathrate hydrate structures.

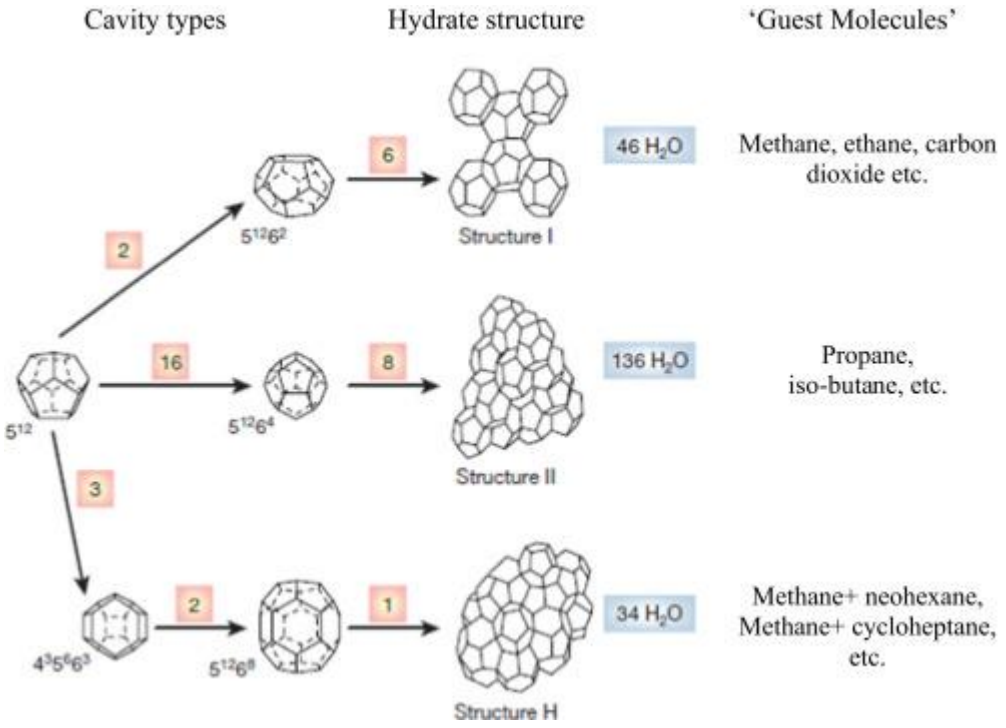

Figure 1-5: The three most common hydrate structures I, II and H. The number above the arrows denote the cavities per unit cell (12)

In type-I hydrate, the structure is formed by two 5^{12} cages and six $5^{12}6^2$ cages with 46 water molecules. In type-II hydrates, the structure is formed by 16 small 5^{12} cavities and eight large $5^{12}6^4$ cages with 136 water molecules. The final structure H is formed by three small 5^{12} cages, two medium $4^35^66^3$ cages, and one large $5^{12}6^8$ cage and 34 water molecules.

Unlike structure I and II which requires one guest molecule, Structure-H require both a small and a larger molecule to remain stable. These larger guest molecules are typically condensate or larger hydrocarbons. The cage size of the hydrate structures is determined by the size of the guest molecule. While methane, the most abundant and important hydrate forming guest molecule may fit into both the small and large cavities of structure sI, propane is too large and will only fit in sII. Methane may also form sII hydrates, but it is less common.

Table 1-1: Properties of the hydrate structures. Average cavity radius varies with temperature, pressure and guest composition (13).

Cavity	sI		sII		sH		
	Small	Large	Small	Large	Small	Medium	Large
Description	5^{12}	$5^{12}6^{2}$	5^{12}	$5^{12}6^{4}$	5^{12}	$4^{3}5^{6}6^{3}$	$5^{12}6^{8}$
No. of cavities/unit cell	2	6	16	8	3	2	1
Average cavity radius (Å)	3.95	4.33	3.91	4.73	3.91C	4.06[c]	5.71[c]
no. of waters/unit cell	46		136		34		

The number of guest molecules occupying the cage structures may be quantified by the hydration number *n.* This describes the amount of water molecules per guest molecule in clathrate hydrates. As an example, if a guest molecule only occupies the large cavities of an sII hydrate, there would be one guest molecules in each of the eight $5^{12}6^{4}$ cages with a total of 136 water molecules. This leads to 17 water molecules per guest molecule, hence a hydration number of 17

1.6 Tetrahydrofuran as hydrate former

Tetrahydrofuran (THF) is an organic heterocyclic polar compound with the formula $(CH_2)_4O$. THF is known to form sII clathrate hydrates with water at atmospheric conditions. THF has been shown to be a useful substitute for methane and CO_2 in hydrate studies that otherwise would require a high-pressure set up, despite being a polar compound. The sheer size of the THF molecule leads to an overall behaviour resembling non-polar fluids in sediments (1). Similar growth patterns are also expected for THF and methane hydrates. This is due to both compounds forming sII hydrates and their hydrates having similar interfacial tensions with water (14). THF is completely miscible with water, and therefore hydrate form without limitations due to diffusion and advection (1). The molecular structure of THF is shown in the following figure.

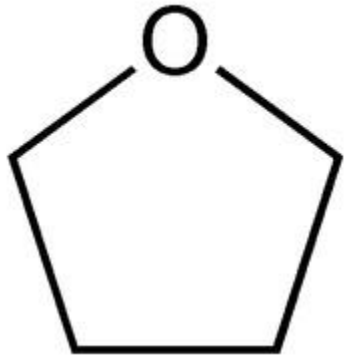

Figure 1-6: Molecular structure of Tetrahydrofuran (15).

The temperature at which THF hydrates form is dependent on the concentration of THF. As a sII hydrate former, THF occupies the larger cages. This leads to eight THF molecules per 136 water molecules and an ideal water/THF mole ratio of 17:1. This is evident in the melting temperature/concentration plot in figure 1-6. The maximum hydrate stable temperature is approximately 4,5°C at a THF mass percent of 19%. A mass percent of 19% translates to a mole ratio of 17:1 water/THF.

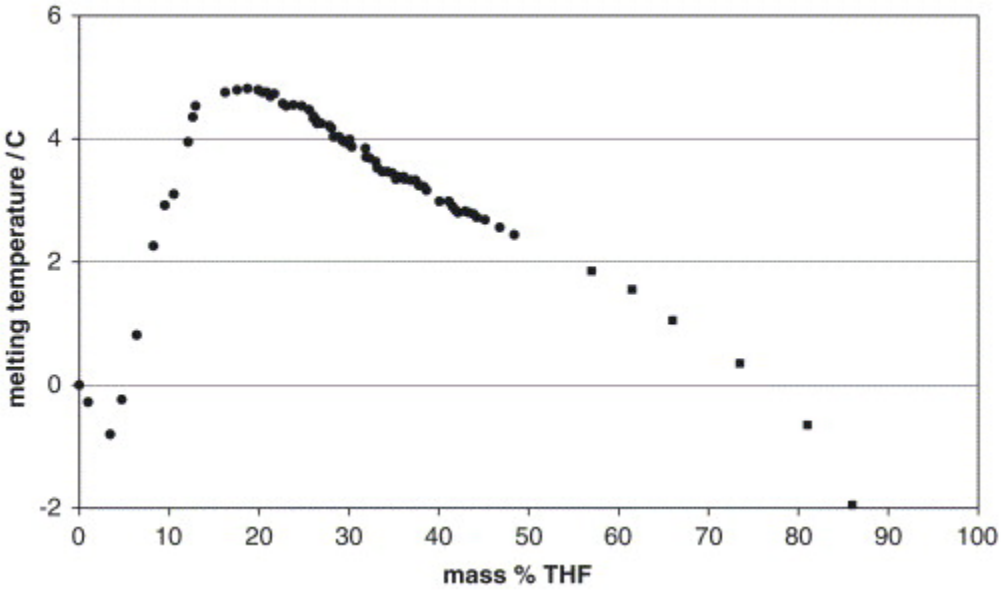

Figure 1-7: Diagram showing the melting temperature of THF-hydrates vs. concentration of THF in solution at 1 atm. A maximum melting temperature of roughly 4,5°C is observed at 19wt% THF (16).

1.7 Hydrate mitigation

There are currently four conventional methods used in the oil and gas industry for gas hydrate inhibition: Heating, depressurization, dehydration, and chemical inhibition. The first two methods rely on avoiding hydrate- stable temperature and pressure conditions. Dehydration is the removal of water content in produced natural gas, and finally chemical inhibitors are substances that may be injected to either slow reaction rates or stop them completely.

Chemical inhibitors are categorized into Thermodynamic hydrate inhibitors (THI) and low dosage hydrate inhibitors (LDHI). THIs are based on organic solvents such as methanol, glycols, and conventional salts such as sodium chloride (NaCl). These inhibitors work by shifting the gas hydrate equilibrium curve towards lower temperature and higher pressures. Organic solvents disrupt the activity of water through hydrogen bonding. This is possible due to organic solvents containing hydroxyl (-OH) groups or free ions causing the coulombic effect. The presence of positive cations and negative anions overpower the effects of hydrogen bonding, disrupting the water structure of hydrates. The downsides of thermodynamic inhibitors are that significant amounts may be required for effective inhibition. In some cases, up to 40wt% or more is required, leading to high operational costs (17).

LDHIs are non-volatile substances that mitigate hydrate growth at significantly lower concentrations than THIs. As LDHIs only require a concentration of 0,5-2,5wt%, they are significantly more beneficial both economically and environmentally. They are categorized into kinetic hydrate inhibitors (KHI) and anti-agglomerates (AAs). KHIs are mostly based on water-soluble polymers that delay hydrate nucleation time. AAs are typically surfactants and quaternary ammonium salts that increase miscibility of components. When the miscibility increases, the solution becomes more stable and single phases do not cluster together.

1.8 Hydrate phase equilibria

A phase diagram is a plot of pressure vs. temperature which describes the equilibrium conditions where various phases of a substance or mixture are present. They are often called pressure-temperature diagrams, or PT-diagrams. The following figure describes the phase equilibrium of mixed THF-CO_2 hydrates with and without the addition of salt inhibitor.

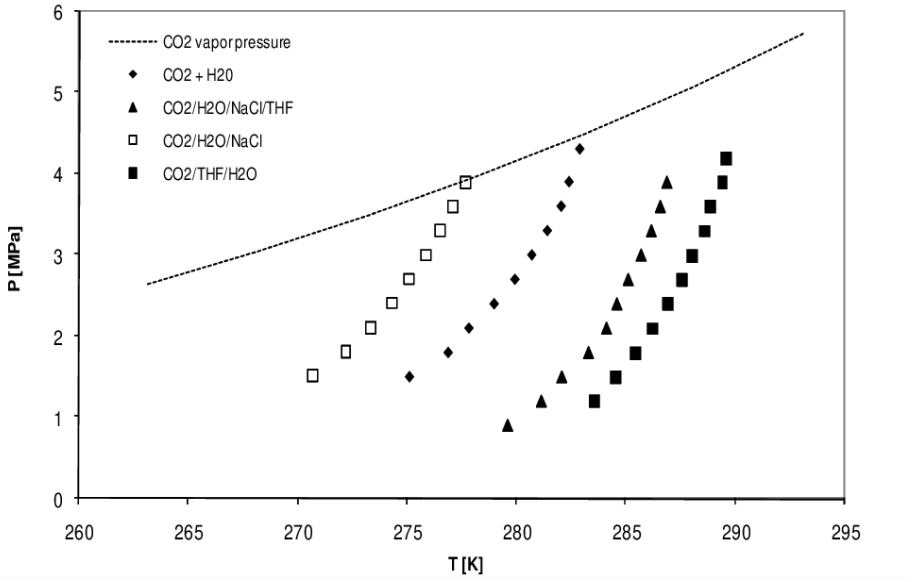

Figure 1-8: Phase diagram showing the equilibrium line of mixed CO_2/THF hydrates with and without salt as an inhibitor (18).

The trends marked by symbols represent the phase boundaries, where hydrates occur to the left of the curve. As an inhibitor is introduced, the phase equilibrium line shifts to lower temperatures. This thesis utilized pure THF hydrate solutions with added salt inhibitors. The phase diagram of CO_2/THF is similar to that of pure THF hydrate but is not completely representative. Solutions containing only THF produce hydrates at 4,5°C at atmospheric conditions, see fig. 1-7.

Hydrate formation is an exothermic process. The formation and dissociation of methane hydrates may be visualized by varying the temperature of a solution in a constant volume agitated autoclave cell shown in figure 1-9. As the solution is cooled, it enters hydrate stable conditions, but does not immediately form hydrates due to metastability (point D). When hydrates nucleate, there is a window of time before the nucleation is macroscopically visible. This time until the appearance of a detectable volume of hydrate is known as the induction time, or lag time. This is represented by the line A to B on the figure. As the temperature decreases, the pressure decreases linearly due to gas solubility and contraction.

At point B, the pressure drops rapidly down to point C as gas is consumed to form hydrates. This releases heat causing a dissociation, which is denoted by the line C-D. Point D is the point of equilibrium.

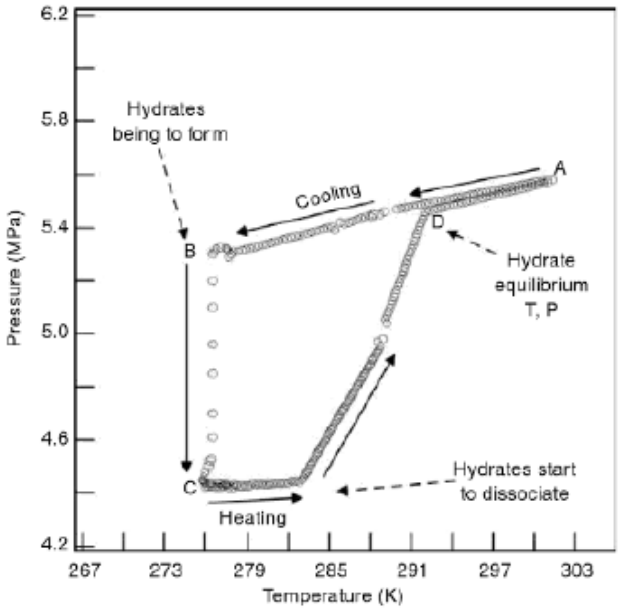

Figure 1-9: P-T diagram showing the methane hydrate formation and dissociation process. Line A-B describes the induction period. Line B-C describes the formation of hydrates. Line C-D describes the dissociation up to the equilibrium point D (13).

1.9 Hydrate growth processes, accumulation, and layering

Disseminated hydrates occur within the pore space of coarse-grained sediments by three common distributions: Pore filling, load bearing and cementation. Pore filling describes the nucleation of hydrates on grain boundaries, growing freely into the pore space. When the hydrate saturation exceeds 25-40%, the hydrates bridge over to neighbouring grains, becoming load bearing. This contributes to mechanical stability. The final distribution behaviour describes the cementation of intergranular contact. This bonds grains together increasing sediment shear and bulk stiffness. The distribution of hydrates is also dependent formation history. In a partial water saturated system, the hydrate prefers to grow at water contacts (11).

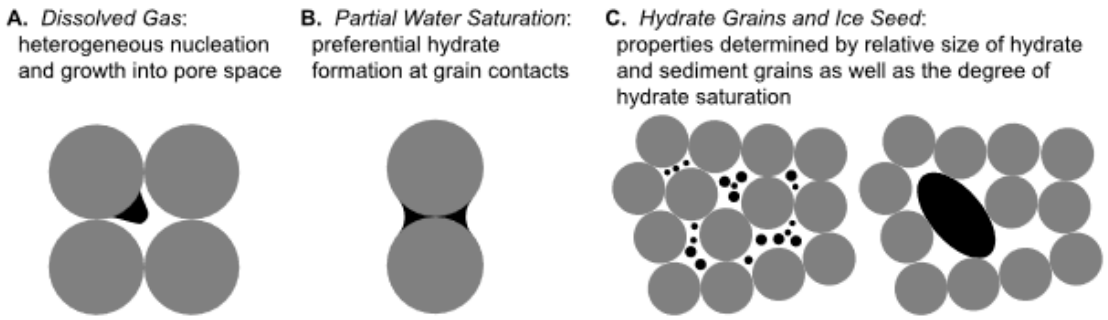

Figure 1-10: Hydrate growth by different formation habits. The distribution of hydrates relative to sediment grains decide the physical properties of hydrate bearing sediments (11).

Earlier studies on hydrates in porous media shows that growth behaviour has a significant dependence on sediment grain size. Non displacive hydrate growth, high permeability and high saturations characterizes coarse-grained sediments. With fine-grained sediments, hydrate growth is inherently displacive with a shifted phase boundary to higher pressures and lower temperatures. Capillary forces and cryogenic suction are dominant forces that compete in the displacement of water in fine-grained sediments. Cryogenic suction is the displacement of water due to pressure differences as ice or hydrates grow in fine grained sediments (1). When subjected to mechanical stress, hydrates in fine-grained sediments instead accumulate into macroscopic lenses, veins, and layers in the sediment, extracting water from the surroundings. As a result, the surrounding sediments are compacted. This compaction is preserved after dissociation (1).

1.10 Magnetic resonance imaging - MRI

MRI is an imaging technique mostly used in radiology to provide detailed three-dimensional pictures of human organs and tissue. It creates images using powerful magnets and computer-controlled radio waves. MRI has recently been extensively applied in the studies of clathrate hydrate formation and dissociation. It provides clear, contrasting images of liquid components and solid hydrates in porous media (19). MRI has been proven to be an excellent tool in the studies of methane recovery and CO_2 sequestration (20), (21).

The MRI instrument consists of four key components: The magnet and shims, gradient fields, radio frequency transmitter and receiver coils and scanner control electronics. There a several types of MRI scanners: Permanent magnets, resistive magnets, open magnets, bore magnets etc. The instrument in use for this thesis is the Bruker Biospec 4,7T 47/40 USR super

conducting magnet with a cylindrical closed bore. USR is short for UltraShield Refrigerated magnet. The coils generating the magnetic field are cooled by surrounding liquid helium to achieve super conductivity (22).

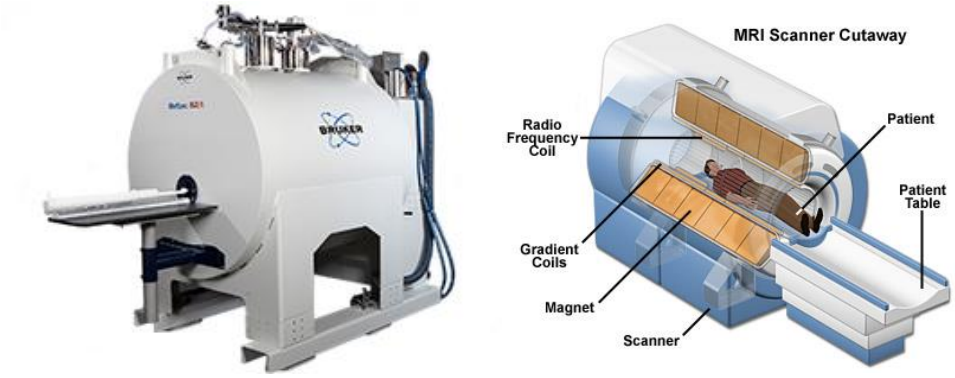

Figure 1-11: The Bruker Biospec 47/40 USR instrument used in this thesis (left) (23), cut-out showing the components of an MRI instrument (right) (24).

1.11 Fundamentals of magnetic resonance imaging

MRI is based on the interaction between an atom that possesses spin and an external magnetic field. A moving electrically charged particle, such as a nucleus of protons and neutrons creates its own magnetic field. It behaves much like a tiny bar magnet spinning around its own axis. The strength of this magnetic field is its magnetic momentum, or spin and is an intrinsic property of elementary particles. Only particles with an odd number of particles in the nucleus possess spin. When particles have an equal number, the opposite spins cancel out. The most basic and important nucleus in MRI is hydrogen, as it is the most abundant element on the planet. Hydrogen only contains one proton in its nucleus, and therefore possesses spin. The following table describes several elements possessing spin, capable of MR imaging:

Table 1-2: Elements possessing spin, their spin quantum number and gyro magnetic ratio (25).

Isotope	Symbol	Spin Quantum number	Gyro Magnetic Ratio (MHz/T)
Hydrogen	^{1}H	1/2	42.6
Carbon	^{13}C	1/2	10.7
Oxygen	^{17}O	5/2	5.8
Fluorine	^{19}F	1/2	40.0
Sodium	^{23}Na	3/2	11.3
Magnesium	^{25}Mg	5/2	2.6
Phosphorus	^{31}P	1/2	17.2
Sulphur	^{33}S	3/2	3.3
Iron	^{57}Fe	1/2	1.4

The spin quantum number indicates the orientation of the intrinsic magnetic momentum of the particles and is measured in integer or half-integer values. An even numbered atomic mass and an odd atomic number will give integer values, while an odd numbered atomic mass gives half-integer values (26). As nature always seeks to exist in the lowest possible energy state, the orientation of the magnetic momentum of particles is in such a way that they cancel each other out when not affected by an external magnetic field. The net magnetization is therefore zero.

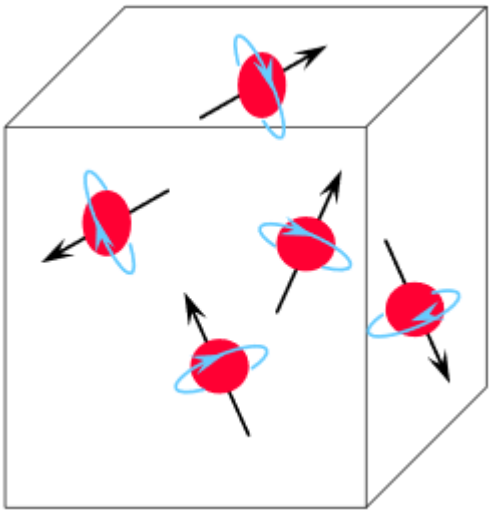

Figure 1-12: Randomly oriented hydrogen particles have a net magnetization of zero in absence of an external magnetic field (25).

When these particles are subjected to an external magnetic field as in MR imaging, they align both parallel and anti-parallel to the magnetic field. These alignments are low energy

and high energy states respectively. The distribution of low and high energy states is not completely equal. There is a tiny excess of low energy state particles. In a 0.5T magnet the amount of excess low energy state particles is 3ppm (parts per million). This number increases as the strength of the external magnetic field does.

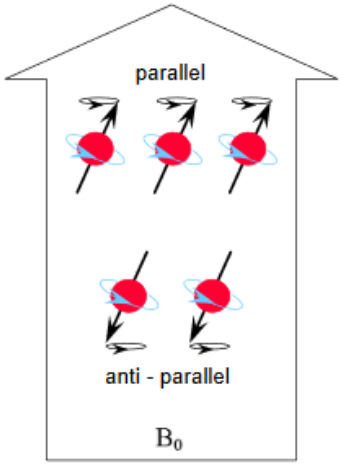

Figure 1-13: Parallel and anti-parallel alignment of particles in an external magnetic field. The magnetic field B_0 operates in the Z-axis. There is an excess of low energy state (parallel) alignments (25).

When exposed to an external magnetic field, the particles precess due to the magnetic momentum. The rate at which they precess is the Larmor Frequency, or Larmor precession.

- $\omega_0 = \gamma B_0$ **(F.1)**

Where ω_0 is the precession rate (MHz), γ is the gyro magnetic ratio of the particle (MHz/T) and B_0 (T) is the external magnetic field strength. The gyro magnetic ratio relates the particle's magnetic moment to its angular momentum and is a given constant for each particle. This ratio is the largest for hydrogen at 42,57 MHz/Tesla (25). The Larmor frequency is the frequency at which a particle will respond to excitation. From this one may find the operating frequency of the MRI system. As an example, the Bruker BioSpec 47/40 USR MRI scanner used in this thesis, has a magnet strength of 4,7T. The Larmor frequency of hydrogen will then be:

- $\omega_0 = 42{,}57 \frac{MHz}{T} * 4{,}7T = \mathbf{200,1MHz}$

This tells us that for this magnet, hydrogen, and only hydrogen will only give a signal when exposed to a radiofrequency of exactly 200,1MHz. When a radiofrequency pulse of a certain amplitude matches the Larmor frequency of the particle of interest, the particle absorbs energy from the pulse. This flips the net magnetization 90° into the transverse plane

and the Z-component of the magnetization, M_z becomes zero. The degree at which the magnetization is flipped is the flip angle (FA). The magnetization may be flipped anywhere between 1°-180° (25).

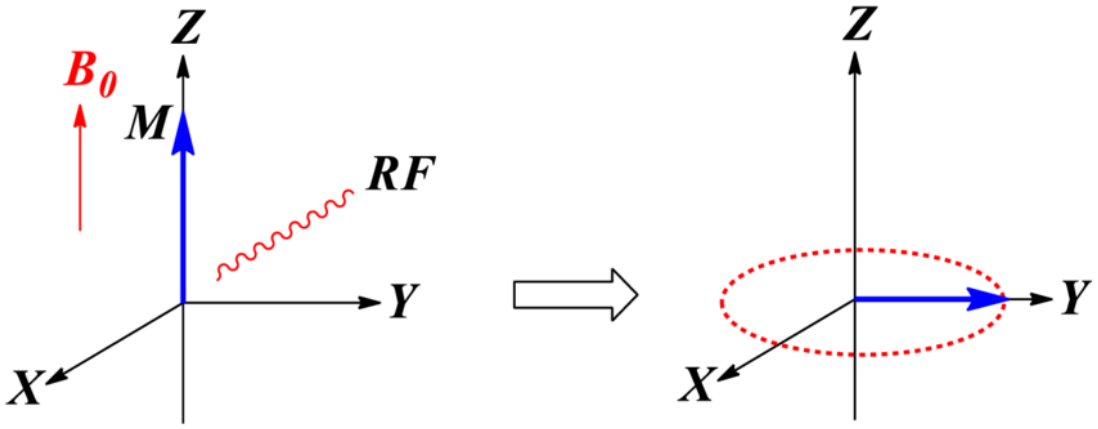

Figure 1-14: The net magnetization in the Z-plane is flipped 90° into the X-Y plane when exposed to a radiofrequency pulse that matches the Larmor frequency of the particle of interest (27)

When the magnetization is flipped into the transverse plane, the particles enter a higher energy state and becomes exited. As they prefer to exist in the state of lowest energy, the particles re-emit the absorbed energy in the form of RF-waves and heat. The M_Z component of the net magnetization then recovers from zero to its equilibrium state at an exponential rate, hence the term relaxation. This relaxation of the net magnetization happens in two separate processes known as T1 and T2 relaxation. These are two completely independent processes, the only thing in common is that they happen simultaneously.

T1 relaxation, also known as Spin-Lattice relaxation, describes the longitudinal component of the process. The term Spin-lattice derives from the fact that energy is released from the system to the surroundings. Not all particles are equally bound to their molecules. For example, hydrogen is bound much tighter in ice than water. The tighter they are bound, the faster the relaxation process. This leads to an uneven bulk relaxation rate. T1 is defined as the time at which 63% of the longitudinal magnetization, M_Z has recovered (25).

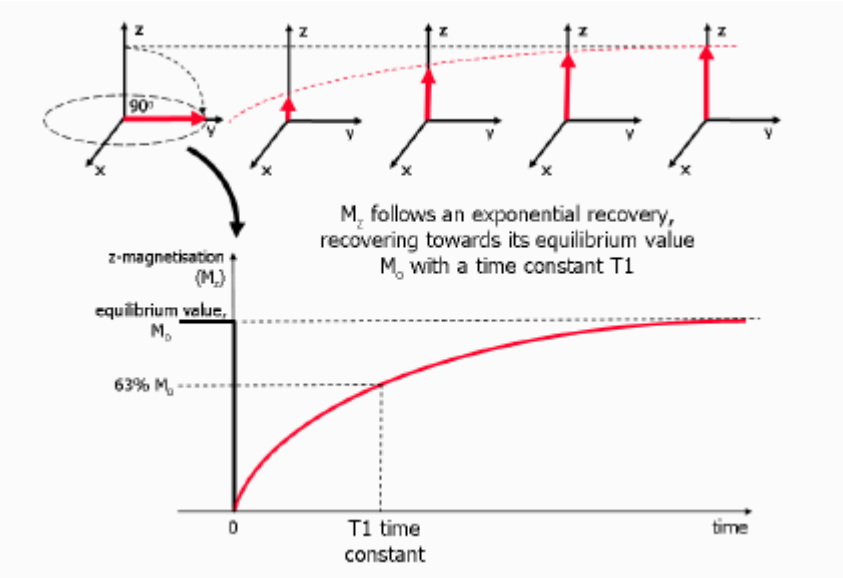

Figure 1-15: T1 gradual relaxation process after a 90° RF-pulse. T1 is the time at which the magnetization in the Z-direction M_z has recovered to 63% of its original value. The time axis is measured in milliseconds (27).

In addition to generating a net magnetization in the Z-plane, particles start to spin in phase when subjected to an external magnetic field. As the particles spin, they constantly attract and repel each other, causing some particles to speed up while others slow down. The particles then start to de-phase until there is no longer any coherence. The process of going from complete in-phase to completely out of phase is the T2 relaxation, or spin-spin relaxation. The name derives from the fact that the particles interact with each other. T2 relaxation is defined as the time at which the net magnetization in the transverse plane, M_{XY} has de-phased to 37% of its original value (25).

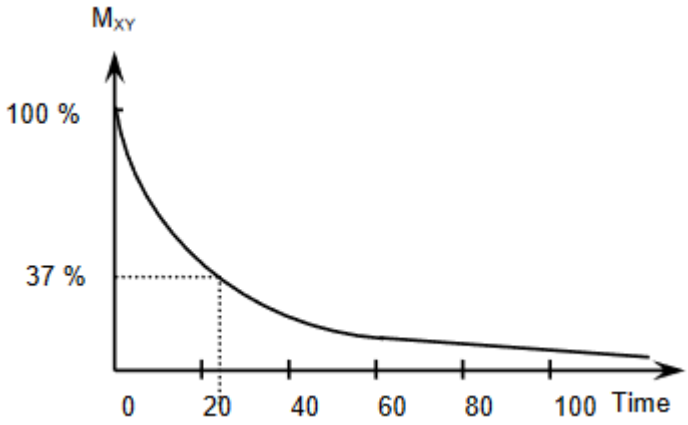

Figure 1-16: Relaxation curve showing the exponential de-phasing of the net magnetization in the XY-plane. T2 is the time at which the magnetization has de-phased to 37% of its original value (25).

The radiofrequency pulse that excites the particles of interest originates from the radiofrequency (RF) coil. The RF-coil may act as both a transmitter and a receiver. As radio waves are electromagnetic radiation, they possess a magnetic component. This magnetic component induces an electric current in copper coils in the RF coil causing a signal. The RF coil must be placed perpendicular to the main magnetic field B_0 to avoid overwhelming the signal from the sample. The MRI scanner is also placed in a faraday cage to avoid picking up external signals leading to noise.

To localize a sample in the MRI instrument, gradient coils are used. Three coils envelop the main magnet, each creating a magnetic field in the X, Y and Z direction. The copper wires are spooled gradually closer together through the magnet to cause a sight gradient in the magnetic field.

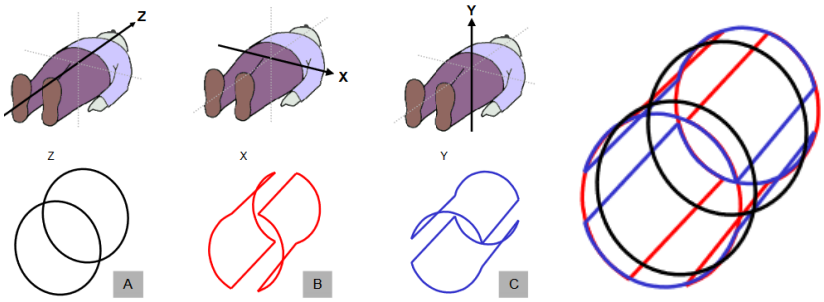

Figure 1-17: Gradient coils produce the gradients G_x, G_y and G_z in the main magnetic field B_0 (25).

In the example of the 4,7T magnet, hydrogen is only exited at a Larmor frequency of 200,1MHz. The gradient coils cause only a single slice in each direction to have a magnetic field strength of exactly 4,7T. When an RF-pulse at 200,1MHz sent into the sample, only the hydrogen in a single voxel will produce a signal. This allows us to map the hydrogen content anywhere in a sample in three dimensions. The signals received by the RF-coil may finally be processed on a computer to produce image slices of the sample.

As the RF coil is placed perpendicular to the magnetic field, it only picks signals from T2 relaxation in the transverse plane. The signal is initially strong, and gradually decays as the relaxation progresses. This is what's known as Free Induction Decay (FID).

As the signal from FID drops very rapidly, free induction decay is difficult to record. An additional 180° RF pulse may be applied to refocus out of phase nuclei. The nuclei then emit an echo signal. The signal is named "echo" as it is rebuilt from the FID. As the nuclei are rephased, one may sample the signal at this moment for the strongest signal. The application

of this 180° pulse is called rephasing. This sequence of pulses is known as the spin-echo sequence. It is the most widely used routine sequence in MRI (25).

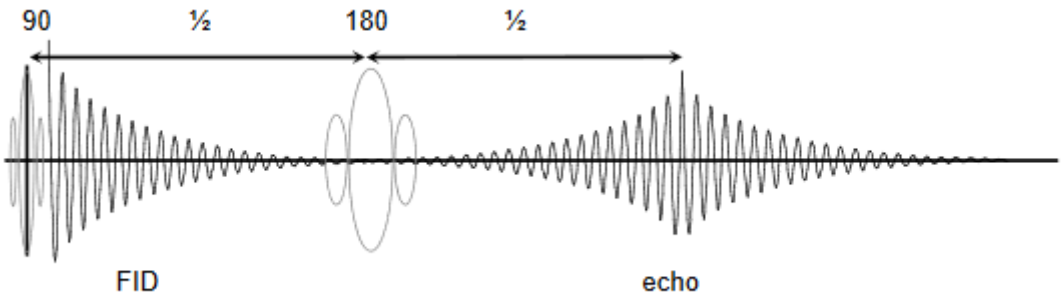

Figure 1-18: Spin-echo sequence showing the 180° rephasing RF pulse and the resulting echo (25).

2 Aim

This objective of this thesis is to observe hydrate formation and layering behaviour in clayey and colloidal silica/quartz sediments in various physical and chemical environments. Hydrate growth is initiated via ice-seeding and progress is recorded via web camera. Tetrahydrofuran (THF) is used as a hydrate former in three different environments: pure distilled water, distilled water with 3,5wt% sodium-chloride and Utsira formation water. This thesis also aims to investigate how hydrate growth and layering is affected by particle size, porosity, and salt as present in marine environments.

MR imaging is also used to observe hydrate formation inside samples via the Fast Spin-Echo protocol (RAREst). When viewing from the outside, hydrate growth is only apparent in the periphery of the samples. As the periphery is in contact with glass, local inhomogeneities cause different growth behaviour when compared to the undisturbed core. MR imaging is therefore proven beneficial, as it allows for a better understanding of the undisturbed hydrate growth. This is especially useful for larger particle size sands such as the Micro5 sand used in this thesis. Larger particle size sands consolidate more strongly, leading to a greater difficulty of observing growth from outside the samples. MR imaging allows one to view the inside in slices throughout the width of the sample.

The first 17 samples aim to investigate how colloidal particle size affects hydrate formation and layering. Samples 23 to 47 aim to observe how growth and layering are

affected by electrolyte content and porosity. The final eight samples employ the MRI instrument to observe hydrate growth behaviour from the within the samples.

3 Methods and experimental procedure

3.1 Chemicals and materials

Table 3-1 describes the various substances used in these experiments. The tetrahydrofuran used in these experiments was inhibitor-free to avoid clouding the solutions. Tetrahydrofuran is known to form explosive peroxides over time, and therefore usually contains an inhibitor such as BHT. To circumvent the problems of an inhibitor-free THF, insoluble solid sodium hydroxide pellets are added to the container.

The distilled water was prepared at The Department of Chemistry at the University of Bergen. Bromothymol blue is a substance with potent colouring properties. It is most often used as a pH indicator. It is yellow at pH values less than 6, green at neutral values, and blue over pH values of 8. This substance has been chosen due to better visibility of the samples on camera.

Utsira formation water is seawater harvested from the Oseberg-South field in the North-sea. The formation water was stored in a freezer at -30ºC shortly after arrival to avoid growth of micro-organisms. It is assumed that it has a salt concentration of roughly 3,2 weight percent. Fleming et al, 2007 suggests that the composition varies dependent on when the sample was taken and from which well (28). In addition to salt, Utsira formation water contains naturally occurring ions. Earlier studies suggest that this ion- content derives from dissolution/precipitation of carbonates and sulphates (29). The constituents of Utsira formation water is shown in table 3-2.

Table 3-1: Table of chemicals and materials used in the experiments, their respective properties, and suppliers.

Substance	Specifications	Supplier	SKU	Particle size	Density (g/cm^3)	Empirical formula	Molar mass (g/mol)
THF	Anhydrous, inhibitor-free >99,9%	Sigma-Aldrich	401757	-	0,889	C_4H_8O	72,11
Distilled water	deionised	Kjemisk Institutt	-	-	0,998	H_2O	18,02
Sodiumchloride	NaCl >99,9%	Sigma-Aldrich	31434	-	1,25	NaCl	58,44
Utsira formation water	3,2wt% electrolytes	Oseberg South Field	-	-	1,023	-	-
Silica	99,80%	Sigma-Aldrich	718483	12nm	2,65	SiO_2	60,08
Silica fumed	99,80 %	Sigma-Aldrich	S5505	0,2-0,3µm	2,65	SiO_2	60,08
Q4 Micro5	High Purity Quartz Filler	Equinor	-	D90 - 11,1 µm D50 - 4,8 µm D10 - 1,0 µm	2,65	SiO_2	60,8
Bromothymol blue	-	Merck Life Science AS	114413	-	2,16	$C_{27}H_{28}Br_2O_5S$	624,38

Table 3-2: Constituents of Utsira formation water (29).

Constituent	Concentration (mg/l)
Na	10728
K	331
Mg	800
Ca	482
Sr	13,2
Ba	0,2
Cl	19400
HCO_3	1090
SO_4	7
pH	6,64

Silica and quartz were chosen for these experiments due to marine clay´s incompatibility with MRI instruments. As marine clay contains magnetic metals, signal is lost due to disturbances in the magnetic field of the MRI instrument. The dimensions of the sands are similar to marine clay and it is therefore used as a substitute. The silica consists of extremely fine particles. Both the 12nm and 0,2-0,3µm particle size silicas create colloidal suspensions in solution. These suspensions are mechanically stable as the settling of sub-micron particle sizes is governed by electrical interparticle forces (30).

The Micro5 is supplied by The Quarts Corp to Equinor. Micro5 is a quartz sand consisting of a particle size distribution as shown in table 2 below. Particle sizes less than 2µm are defined as clay particles, from 2-6µm as silt, and above 6µm as sands. This describes Micro5 as a sand containing roughly 50% silt with a small percentage of clay particles. Micro5 quartz sand also contains traces of metal ions. The chemical content is described in table 3 below.

Table 3-3 and 3-4: Particle size distribution of Micro5 sand as stated by The Quartz Corp (left) and it's chemical content in parts per million (right).

Particle size distribution (µm)	
	Typical value
D10	1,0
D50	4,8
D90	11,1

Chemical content	
	Typical value (ppm)
Al	14,4
Ca	3,1
Fe	0,7
K	1,5
Li	0,4
Na	1,5
Ti	1,2

It is of uttermost importance that the safety precautions of handling fine silica and quartz are not understated. When handling microscopic silica, one must use respiratory masks with compatible filters and combined nitrile-neotop gloves. Skin contact should be avoided, and open containers should always be handled in fume hoods. Silica is a known carcinogenic and inhalation may cause permanent respiratory damage.

3.2 Sample preparation

Bulk solutions of roughly 17:1 mole ratio of water and THF were made to supply the hydrate/water mixtures as shown in table 3-5 below. To better visualize the crystallization of hydrates, bromothymol blue was added to colour later samples. Several bulk solutions were made with pure distilled water and THF. The salt containing bulk solution was made by adding salt to one of the pure bulk solutions. The Utsira formation water was collected 16.01.18 and stored in a freezer 23.01.18. It was melted on the 31.01.20 when the first Utsira formation water samples were prepared.

Table 3-5: Table of bulk distilled water/THF solutions with 17:1 mole ratio.

Bulk sample	Water volume (ml)	THF volume (ml)	Total volume (ml)	Solution density (g/cm3)	Bromothymol mass (g)	Bromothymol blue concentration (ppm)	NaCl mass (g)
Distilled water/THF	612,5	162,0	774,5	0,967	0,005	8	-
17:1 THF/H_2O with NaCl	-	-	293,3	1,004	0,01	43	10,5
Utsira Formation water	189,0	50,0	239,0	0,978	0,01	43	-

The samples for the visual analysis of hydrate growth in silica sediments and their respective coding are presented in table 3-6. They are presented by the following structure: Particle size- salt content- colouring content- sample number. For the particle size, ***M5*** denotes the Micro5 Quartz filling with a distribution as shown in table 3-3. Salt content is either denoted as ***D***- Pure distilled water/THF solution, ***3,5%***- 3,5 weight percent NaCl in distilled water/THF solution, or ***U***- Utsira formation water/THF solution containing roughly 3,2 weight percent NaCl. The colouring is either denoted ***NC***- No colouring, or ***C***- colouring.

As an example, the first sample is denoted as 12nm-D-NC-1, where 12nm indicates the particle size, D denotes pure distilled water/THF solution, NC is no colouring and 1 is the sample number.

Table 3-6: Table of samples for the visual analysis of hydrate growth in sediments, their respective coding, and the date they were prepared.

Date	Sample No.	Sample code	Date	Sample No.	Sample code
07.01.20	1	12nm-D-NC-1	30.01.20	24	0,3um-3,5%-C-1
08.01.20	2	12nm-D-NC-2	30.01.20	25	0,3um-3,5%-C-2
14.01.20	3	12nm-D-NC-3	30.01.20	26	0,3um-3,5%-C-3
15.01.20	4	12nm-D-NC-4	30.01.20	27	0,3um-3,5%-C-4
18.01.20	5	12nm-D-NC-5	30.01.20	28	0,3um-3,5%-C-5
07.01.20	6	0,3um-D-NC-1	30.01.20	29	0,3um-3,5%-C-6
08.01.20	7	0,3um-D-NC-2	01.02.20	30	0,3um-U-C-1
15.01.20	8	0,3um-D-NC-3	01.02.20	31	0,3um-U-C-2
18.01.20	9	0,3um-D-NC-4	01.02.20	32	0,3um-U-C-3
21.01.20	10	0,3um-D-NC-5	01.02.20	33	0,3um-U-C-4
21.01.20	11	12nm-D-C-test	01.02.20	34	0,3um-U-C-5
22.01.20	12	12nm-D-C-1	01.02.20	35	0,3um-U-C-6
22.01.20	13	12nm-D-C-2	14.02.20	36	M5-D-C-1
22.01.20	14	12nm-D-C-3	14.02.20	37	M5-D-C-2
22.01.20	15	0,3um-D-C-1	24.02.20	42	M5-D-C-3
22.01.20	16	0,3um-D-C-2	24.02.20	43	M5-D-C-4
22.01.20	17	0,3um-D-C-3	14.02.20	38	M5-3,5%-C-1
28.01.20	18	0,3um-D-C-4	14.02.20	39	M5-3,5%-C-2
28.01.20	19	0,3um-D-C-5	24.02.20	44	M5-3,5%-C-3
28.01.20	20	0,3um-D-C-6	24.02.20	45	M5-3,5%-C-4
28.01.20	21	0,3um-D-C-7	14.02.20	40	M5-U-C-1
28.01.20	22	0,3um-D-C-8	14.02.20	41	M5-U-C-2
28.01.20	23	0,3um-D-C-9	24.02.20	46	M5-U-C-3
			24.02.20	47	M5-U-C-4

Samples were prepared by filling 80ml clear sample vials to the brim with silica. Roughly 50ml of the 17:1 mole ratio THF/water solution was then added by a 25ml syringe. The samples were homogenized on a magnetic stirrer to avoid aggregates of silica. After stirring, the magnet was removed by guiding it with another magnet on the outside of the vials.

The rest of the samples are prepared using a quantitative approach. More precise measurements were made for the weight of the silica/quartz and water/THF solution to give an estimation of the sample pore volume. A Kern EG420-3NM Scale with an accuracy of ±0,01g was used to weigh in exact amounts of silica and quartz. A known amount of water/THF solution was also weighed to find the density of each solution. This density could

then be used to find the exact liquid volume by the total sample weight. A more complete table of sample dimensions may be found in the results section.

For the MR imaging experiments, the same sample vials were used. 17:1 bulk solutions of distilled water/inhibitor free THF was prepared in the same manner as previously stated at Equinor Sandsli. The following table describes the samples and coding for the MRI experiments.

Table 3-7: Table of samples and their respective coding for the MRI experiments.

Date	Sample No.	Sample code
03.03.2020	48	MA1
03.03.2020	49	MA2
10.03.2020	50	MRI-M5-D-1
10.03.2020	51	MRI-M5-D-2
14.02.2020	52	MRI-M5-U-1
14.02.2020	53	MRI-M5-U-2
13.03.2020	54	MRI-M5-U-3
13.03.2020	55	MRI-M5-U-4

The samples follow the same coding as previously stated. Samples 50 and 51 were made by re-using samples 40 and 41 to allow for faster preparation. They were heated to 50℃ and homogenized to avoid hydrate memory effects. The samples were then left to settle for three days before scanning. For samples 52 and 53, a new batch of Utsira formation water was used. This was melted 09.03.20.

Samples 48 and 49 were prepared by freezing to -18℃ overnight. The following day they were moved to another freezer set to 3,5℃. This was to ensure there was no ice present in the samples. Samples 48,49, 52 and 53 were to be prepared using the same ice-seeding procedure as the previous sets of experiments.

3.3 Visual analysis experimental setup

To observe hydrate growth, a Logitech C922 Pro web camera was used to continuously record the process. The experimental set-up is as shown in the following two figures.

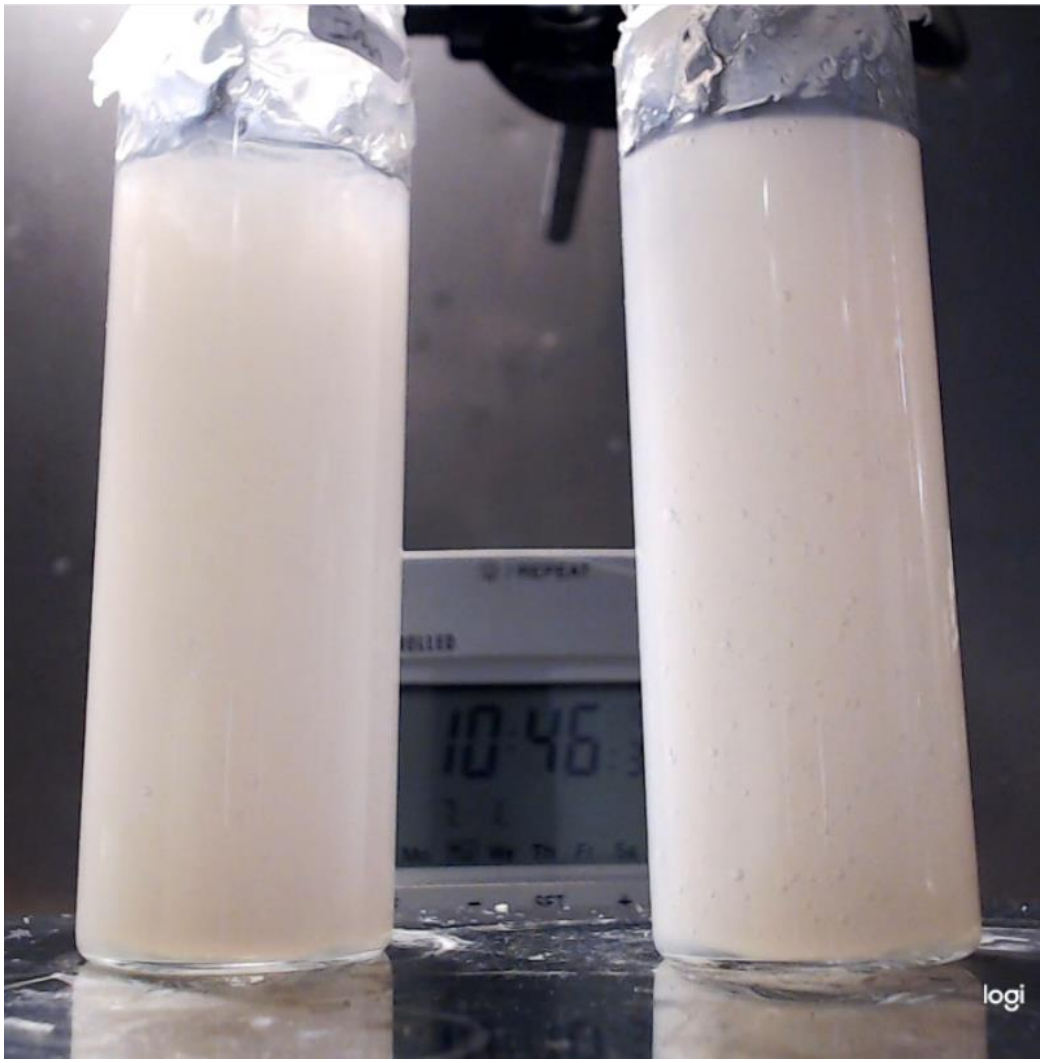

Figure 3-1: Experimental set-up used for the first samples 11 as seen through the web camera. Two samples are recorded simultaneously. A PT-100 temperature sensor is submerged into the sample from the top, and parafilm is used to seal it.

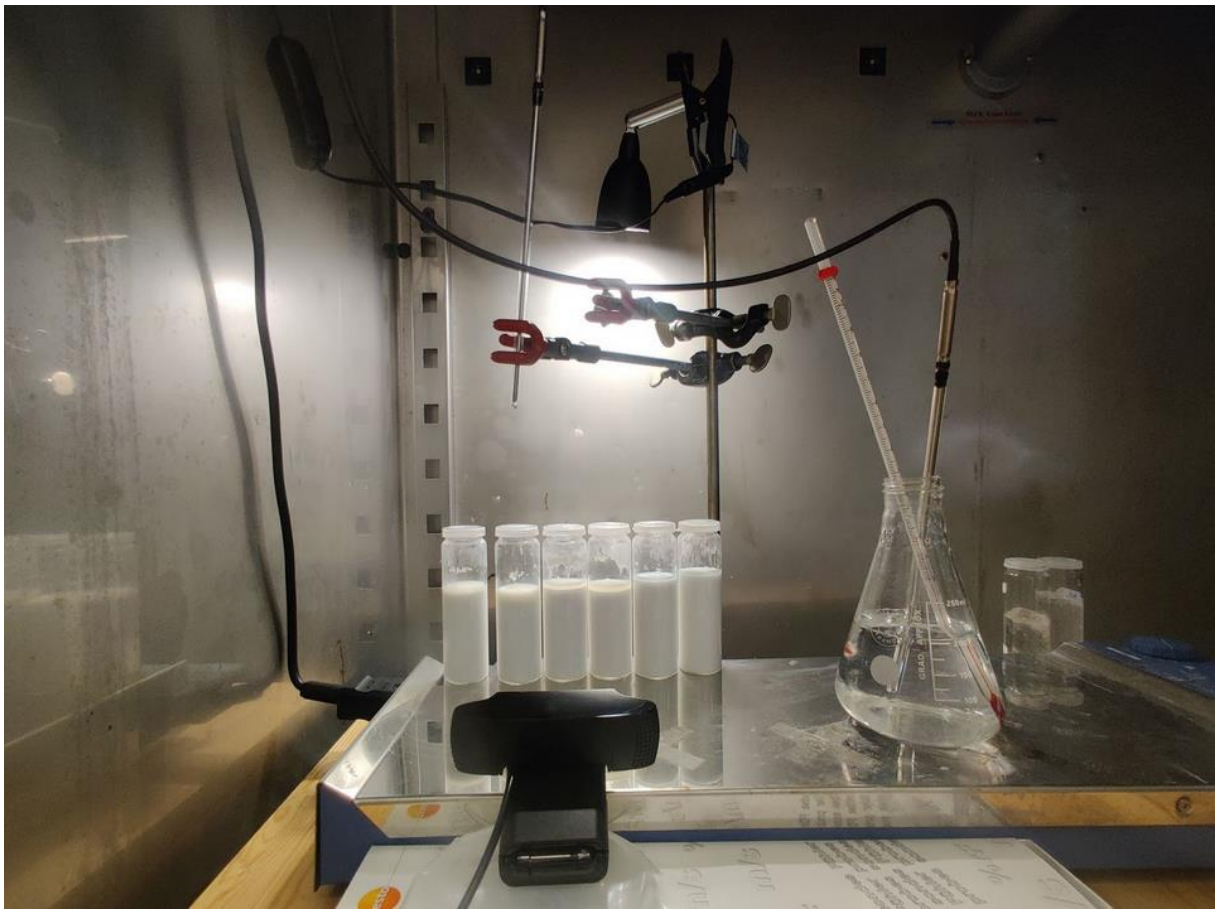

Figure 3-2: Experimental set-up of the remaining samples. Six samples are recorded simultaneously. A PT-100 temperature sensor is submerged into a separate container of water and NaCl to measure the temperature in the freezer. A LED lamp is used to provide backlight behind samples.

The samples were cooled and stored in a Mastercella Carel freezer. To record the temperature in the freezer, a Testo 176-T4 data logger was used. Two PT-100 type sensors with an accuracy of ±0,3ºC were connected to the data logger. The samples containing 12nm and 0,2-0,3µm silica were prepared a day in advance of the experiments. Unlike the colloidal silica, the Micro5 quartz filling does not remain in suspension due to its larger particle size. Compaction was still observed several days after settling, forcing solution to the top of the sample. The compaction results in a solid unmoveable mass of quartz. The Micro5 samples were therefore left to settle for three days before experiments were performed. Excess water/THF solution was kept in the sample to help initiate the nucleation.

All samples were stored in the freezer a few hours before initiating the experiments to ensure hydrate stable conditions. The hydrate nucleation was initiated by seeding 0,5-1g grains of ice at temperatures well within the hydrate stable phase-boundary. The ice was submerged completely under the surface of the sample using a tweezer.

For the first 11 samples the temperature was set to 3,5ºC. The web camera's proprietary software Logitech Capture was used to record the samples continuously. One sample of each silica particle size was recorded simultaneously with temperature sensors submerged in each sample. Each experiment was then run for 24 hours. The capture software allowed for continuous footage for 5 hours, before overwriting the start of the recording. This inevitably led to some data loss and is the reason the remaining samples follow a different procedure.

For next six samples, bromothymol blue was added as colouring and the new experimental set-up was tested. This set-up was then used for the remaining samples. From sample 18 and onwards, the freezer temperature was lowered to 0ºC to ensure the nucleation of hydrates in salt containing samples. Six samples were recorded simultaneously with Windows 10´s included camera software. Two with pure distilled water, two with 3,5 weight percent salt and two with Utsira formation water. The time lapse function was used to take a picture every 10 seconds for 48 hours. This method was chosen due to higher fidelity and less cumbersome data management. After finishing the experiments, the data could then easily be reduced. A single temperature sensor was kept in a separate glass of water to exclude uncertainties due to nucleation on the sensors. Salt was added to the water with the sensor to avoid freezing at sub-zero temperatures.

3.4 MRI configuration and procedure

Figure 3-3 illustrates the layout of the MRI laboratory at Equinor's office at Sandsli. Both the magnet room and the whole laboratory act as faraday cages to block external RF signals. The operator area houses a Linux-based computer that controls the MRI instrument and other peripheries. The computer processes signals through Bruker's software Paravision 6.0. The technical room consists of the MRI instruments power supply, cooling equipment, and other technical equipment.

To avoid magnetic emergencies where any person may be injured due to magnetic forces, a quench system exists. Pressing an emergency button will cause the liquid helium to be quickly removed from the MRI instrument. This de-energizes the magnet within seconds to minutes. There are two emergency buttons. One in the MRI room, and one at the operator area.

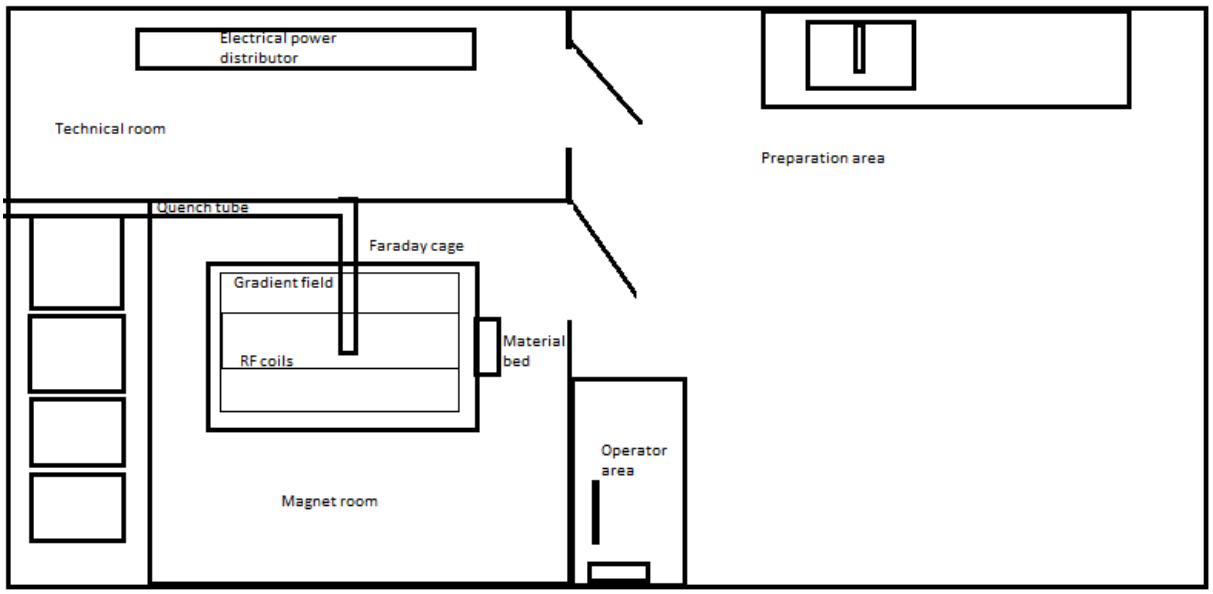

Figure 3-3: Graphic showing the MR imaging lab at Equinor Sandsli. Both the whole laboratory and the magnet room act as faraday cages to block external RF signals. The MR imaging instrument is a superconducting closed bore cylindrical magnet cooled by liquid helium. The quench tube is an emergency system that removes the liquid helium out of the instrument. The operator area consists of a computer that controls the MRI instrument and processes data. The technical room consists of the power supply and cooling equipment (22).

Paravision 6.0 is the user interface for the operation of Bruker's MRI instruments. It is used for acquisition control, data reconstruction, data evaluation and archiving. The software is preinstalled and configured to the specific MRI scanner by Bruker upon delivery of the instrument (22). The data received from the MRI imaging is archived in the following Hierarchy:

1. Subject
2. Study
3. Image series

Image series are the individual scans in a specific study where the name starts at E0 and increases for each individual scan. The study contains the all the image series for each specific sample. The subject is the main folder containing all studies.

The imaging technique used for scans in this thesis is the RAREst protocol. RAREst is short for Rapid Acquisition with Refocused Echoes for short echo time, also known as Fast Spin-Echo (FSE). This technique is based on the spin-echo sequence, but instead of only having a single rephasing pulse, it has multiple. By applying a different phase encoding gradient to each echo, multiple k-space lines may be filled simultaneously. The advantage of

using RAREst is that it is sped up compared to the conventional spin-echo sequence. The speed-up factor is equal to the number of rephasing pulses (31).

Before initiating a scan, a set of procedures must be performed. These procedures include the shimming-, wobble- and localizer- procedure as described below:

Magnetic properties may vary in different regions of a sample. As it is placed into the static magnetic field of the MRI instrument, local variations in the magnetic field strength may appear. This is known as susceptibility effects. This effect may be partially compensated for by shim coils. Shimming the sample attempts to homogenize the field specifically for each sample. For every new study, an automatic shimming is performed (22).

When the load of the sample has been changed between consecutive studies, tuning and matching of the RF-coils is required. Tuning and matching is done through the wobble procedure in Paravision. When tuning, the resonance frequency of the coil is shifted, and the coil impedance is calibrated to match the impedance of the transmission chain. This reduces the reflection of radio frequency power during transmission and increases the sensitivity during signal reception (22).

The localizer procedure is a quick, low resolution and large field of view scan that produces an image in the X, Y and Z plane. These images allow one to find the sample inside the MRI instrument and decide the region of interest (ROI). The image slicing may then be adjusted accordingly. The localizer procedure is performed with the Localizer_RARE_Multislice command in Paravision using Bruker's default settings.

Before initiating a RAREst scan, the following parameters must be set:

- Field of view (FOV): The field of view defines the imaging area inside the MRI instrument.
- Image size: The image size determines the resolution of the produced image. A higher resolution leads to more pixels in each image.
- Number and orientation of slices: The MRI instrument produces image slices of arbitrary thickness in the orientation of choice. Figure 2-4 illustrates the three planes of motion used in MR imaging. Slices in the transverse and sagittal plane are numbered from one side to the other, while slices in the coronal plane are numbered from the bottom to the top of the sample. It is important that there are no slice gaps or overlap between the slices for optimal imaging.

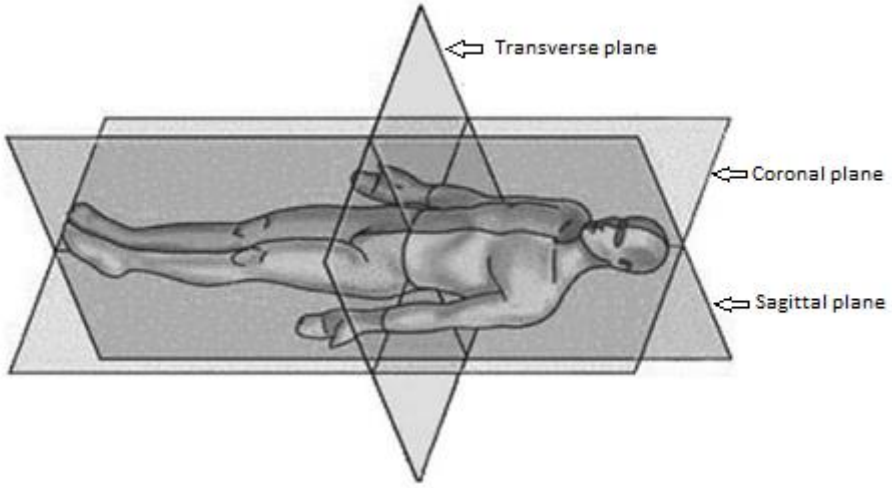

Figure 3-4: Plane orientations in MR imaging.

- Repetition time, TR: The repetition time, TR describes the time between each applied 90° RF-excitation pulse in milliseconds (32).
- Averages: The “averages” parameter allows one to set the amount of scan repetitions before an average value is determined. A higher amount of averages leads to a better signal, but also increases scan time.
- Echo time, TE: The echo time, TE describes the time in milliseconds between the application of an RF excitation pulse and the peak of the signal induced in the reciever coil (33).
- Echo spacing: The echo spacing is the time between the echoes, or signal response after a 180° rephasing pulse. A longer echo spacing allows for longer echo times, but affects signal to noise ratio and contrast to noise ratio negatively (32).
- Rare factor: The rare factor determines how many refocusing pulses are applied after the initial excitation RF-pulse (31).

4 Results

4.1 Sample overview for hydrate growth- and MRI experiments

The following section shows three tables describing the properties of all samples in their respective experiment runs. Table 4-1 describes analysis of colloidal silica suspensions and the testing the addition of colouring. Table 4-2 describes the experiments visualizing hydrate growth in both colloidal and a clay/sand mixture with varying electrolyte compositions and porosities. Table 4-3 describes the samples prepared for MRI screening. The samples are identified by the following coding structure: Particle size- salt content- colouring content- sample number. Colouring is omitted for the MRI experiments as it is not required for better visibility. This also excludes uncertainties of the interaction between colouring and hydrate growth.

Table 4-1: Table of the qualitative sample results using the prior set-up (sample 1-10), the bromothymol blue colouring test sample (sample 11) and the samples testing the new set-up (sample 12-17).

Date	Sample No.	Sample code	THF/H2O volume (ml)	Colouring (ppm)	Hydrate growth	Sample temperature (±0,5°C)
07.01.20	1	12nm-D-NC-1	50	0	Yes	3,5
08.01.20	2	12nm-D-NC-2	50	0	no	3,5
14.01.20	3	12nm-D-NC-3	50	0	yes	3,5
15.01.20	4	12nm-D-NC-4	50	0	yes	3,5
18.01.20	5	12nm-D-NC-5	50	0	yes	3,5
07.01.20	6	0,3um-D-NC-1	50	0	yes	3,5
08.01.20	7	0,3um-D-NC-2	50	0	yes	3,5
15.01.20	8	0,3um-D-NC-3	50	0	yes	3,5
18.01.20	9	0,3um-D-NC-4	50	0	yes	3,5
21.01.20	10	0,3um-D-NC-5	50	0	no	3,5
21.01.20	11	12nm-D-C-test	50	0	yes	3,5
22.01.20	12	12nm-D-C-1	50	15	yes	3,5
22.01.20	13	12nm-D-C-2	50	15	yes	3,5
22.01.20	14	12nm-D-C-3	50	15	yes	3,5
22.01.20	15	0,3um-D-C-1	50	15	yes	3,5
22.01.20	16	0,3um-D-C-2	50	15	yes	3,5
22.01.20	17	0,3um-D-C-3	50	15	yes	3,5

Table 4-2: Table of quantitative samples, when they were prepared and their respective volumes, masses, porosities, and nucleation temperatures.

Date	Sample No.	Sample Code	Hydrate growth	THF/H2O volume (ml)	Solid mass (g)	Solid volume (ml)	Total mass (g)	Total volume (ml)	Porosity	Colouring concentration (ppm)	Sample temperature (±0,5°C)
28.01.20	18	0,3um-D-C-4	yes	47,78	2,95	1,11	49,13	48,89	0,98	8	2,0
28.01.20	19	0,3um-D-C-5	yes	47,98	2,58	0,97	48,95	48,95	0,98	8	-0,5
28.01.20	20	0,3um-D-C-6	yes	48,82	2,82	1,06	50,00	49,88	0,98	8	-0,5
28.01.20	21	0,3um-D-C-7	yes	28,86	2,84	1,07	30,73	29,93	0,96	8	2,0
28.01.20	22	0,3um-D-C-8	yes	28,66	2,78	1,05	30,48	29,71	0,96	8	-0,5
28.01.20	23	0,3um-D-C-9	yes	28,61	2,85	1,08	30,50	29,68	0,96	8	-0,5
30.01.20	24	0,3um-3,5%-C-1	no	49,70	2,78	1,05	52,68	50,75	0,98	8	2,0
30.01.20	25	0,3um-3,5%-C-2	yes	49,92	2,73	1,03	52,85	50,95	0,98	8	-0,5
30.01.20	26	0,3um-3,5%-C-3	yes	47,56	2,78	1,05	50,53	48,61	0,98	8	-0,5
30.01.20	27	0,3um-3,5%-C-4	no	27,28	2,82	1,06	30,21	28,35	0,96	8	2,0
30.01.20	28	0,3um-3,5%-C-5	yes	29,47	2,88	1,09	32,47	30,56	0,96	8	-0,5
30.01.20	29	0,3um-3,5%-C-6	yes	29,30	2,87	1,08	32,29	30,39	0,96	8	-0,5
01.02.20	30	0,3um-U-C-1	no	52,04	2,70	1,02	53,60	53,06	0,98	43	2,0
01.02.20	31	0,3um-U-C-2	yes	50,59	2,92	1,10	52,40	51,69	0,98	43	-0,5
01.02.20	32	0,3um-U-C-3	yes	51,18	2,78	1,05	52,83	52,22	0,98	43	-0,5
01.02.20	33	0,3um-U-C-4	no	30,26	2,73	1,03	32,32	31,29	0,97	43	2,0
01.02.20	34	0,3um-U-C-5	yes	31,09	2,79	1,05	33,20	32,15	0,97	43	-0,5
01.02.20	35	0,3um-U-C-6	yes	31,92	2,93	1,11	34,15	33,03	0,97	43	-0,5
14.02.20	36	M5-D-C-1	yes	26,66	40,80	15,40	66,57	42,06	0,63	8	0,0
14.02.20	37	M5-D-C-2	yes	22,83	38,13	14,39	60,20	37,22	0,61	8	0,0
24.02.20	42	M5-D-C-3	yes	26,66	40,80	15,40	66,57	42,06	0,63	8	0,0
24.02.20	43	M5-D-C-4	yes	22,83	38,13	14,39	60,20	37,22	0,61	8	0,0
14.02.20	38	M5-3,5%-C-1	yes	26,86	42,82	16,16	69,79	43,02	0,62	8	0,0
14.02.20	39	M5-3,5%-C-2	yes	27,19	40,81	15,40	68,11	42,59	0,64	8	0,0
24.02.20	44	M5-3,5%-C-3	yes	26,86	42,82	16,16	69,79	43,02	0,62	8	0,0
24.02.20	45	M5-3,5%-C-4	yes	27,19	40,81	15,40	68,11	42,59	0,64	8	0,0
14.02.20	40	M5-U-C-1	yes	28,48	45,55	17,19	73,40	45,67	0,62	43	0,0
14.02.20	41	M5-U-C-2	yes	29,39	46,16	17,42	74,90	46,81	0,63	43	0,0
24.02.20	46	M5-U-C-3	yes	28,48	45,55	17,19	73,40	45,67	0,62	43	0,0
24.02.20	47	M5-U-C-4	yes	29,39	46,16	17,42	74,90	46,81	0,63	43	0,0

Sample series 0,3µm-D-C denotes colloidal silica with a 17:1 mole ratio THF/distilled water solution. Series 0,3µm-3,5%-C denotes the addition of 3,5 weight percent salt, and 0,3µm-U-C denotes samples containing Utsira formation water instead of distilled water. Utsira formation water has an electrolyte concentration of roughly 3,2 weight percent. Series M5-D-C, M5-3,5%-C and M5-3,5%-U present the same chemical environments with Micro5 sand instead of colloidal silica.

Table 4-3: Table of samples for MR imaging, when they were prepared and their respective volumes, masses, porosities, and nucleation temperature.

Date	Sample No.	Sample code	Hydrate growth	THF/H2O volume (ml)	Solid mass (g)	Solid volume (ml)	Total mass (g)	Total volume (ml)	Porosity	Sample temperature (±0,5°C)
03.03.2020	48	MA1	no	6,94	17,88	6,75	24,59	13,7	0,51	3,5
03.03.2020	49	MA2	no	6,59	17,76	6,70	24,13	13,3	0,50	3,5
10.03.2020	50	MRI-M5-D-1	yes	15,48	55,86	21,08	70,82	36,6	0,42	2,0
10.03.2020	51	MRI-M5-D-2	yes	18,43	50,87	19,20	68,68	37,6	0,49	2,0
14.02.2020	52	MRI-M5-U-1	yes	22,43	45,55	17,19	67,48	39,6	0,57	0,5
14.02.2020	53	MRI-M5-U-2	yes	24,35	46,16	17,42	69,97	41,8	0,58	0,5
13.03.2020	54	MRI-M5-U-3	yes	21,97	55,20	20,83	76,69	42,8	0,51	0,5
13.03.2020	55	MRI-M5-U-4	yes	21,50	55,76	21,04	76,79	42,5	0,51	0,5

Sample MA1 and MA2 were prepared in an attempt to grow hydrates by freezing and thawing. The samples were left in a freezer at -18°C over-night, before being moved into another freezer set to 3,5°C. This was to ensure there was only hydrates left in the sample. This was a less time-consuming method, but no significant hydrate growth was observed. The remaining six samples instead employed the method of nucleation by ice seeding. The temperature was kept at 2,0°C for samples with no salt, and 0,5°C for the samples Utsira formation water.

4.2 Hydrate growth in colloidal silica suspensions

The following section shows the progressive crystallization of THF/water hydrates in silica over a period of 24-48 hours. It was attempted to keep the time stamps consistent, but this was not possible for all the samples due to limitations of the software. Windows 10 would only allow for roughly 5 hours of continuous capture. If recording exceeded 5 hours, the software would overwrite the start of the recording. Some data was unfortunately lost to this. This problem was solved for later samples by switching to the Windows 10 camera software.

Figures 4-1 to 4-9 show the progressive crystallization of 17:1 mole ratio THF/water hydrates in colloidal silica. The samples were nucleated by ice seeding at 3,5°C. The transparent regions show hydrate crystal growth having displaced silica.

Figure 4-1: Hydrate growth of sample 12nm-D-NC-1 over a 24-hour period.

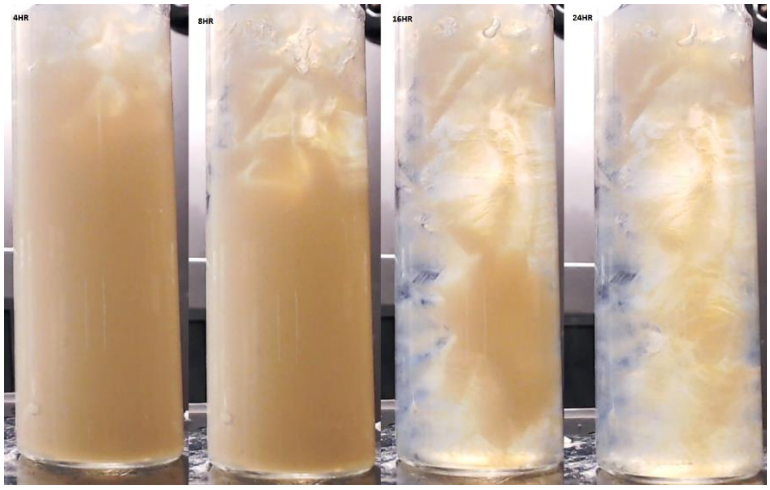

Figure 4-2: Hydrate growth of sample 12nm-D-NC-3 over a 24-hour period. The colour discrepancy is due to contrast changes in the camera software.

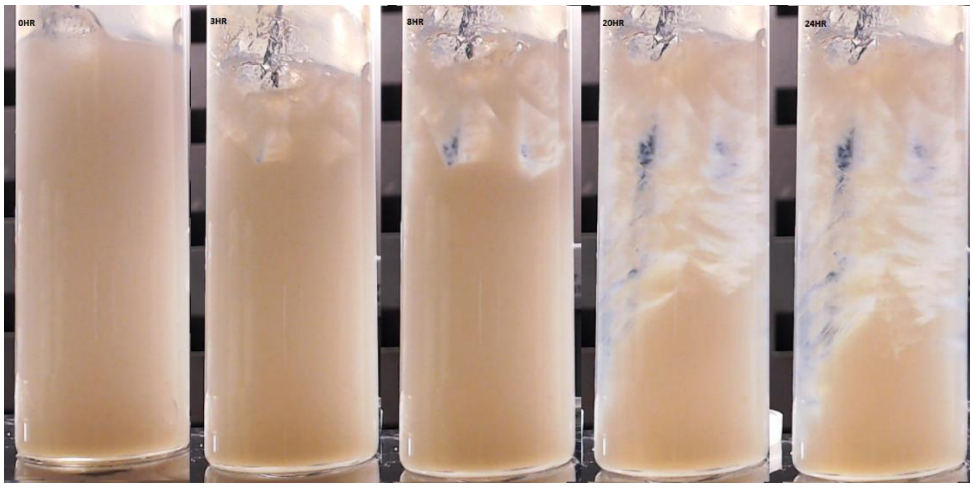

Figure 4-3: Hydrate growth of sample 12nm-D-NC-4 over a 24-hour period.

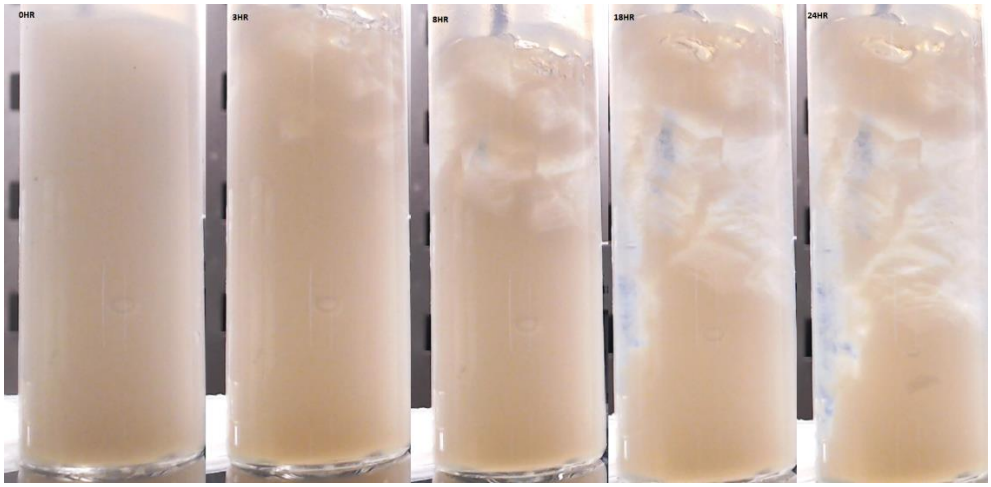

Figure 4-4: Hydrate growth of sample 12nm-D-NC-5 over a 24-hour period.

Figure 4-5: Hydrate growth of sample 0,3µm-D-NC-1 over a 24-hour period.

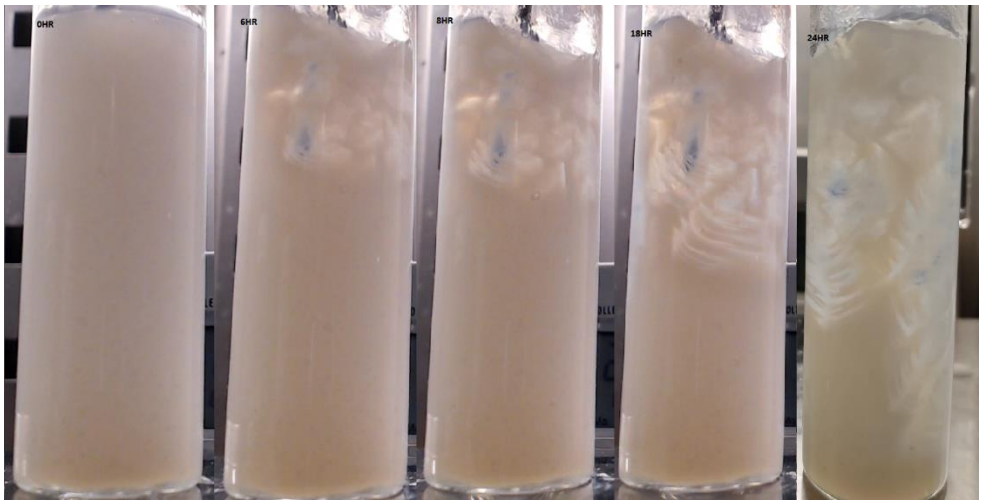

Figure 4-6: Hydrate growth of sample 0,3µm-D-NC-2 over a 24-hour period.

Figure 4-7: Hydrate growth of sample 0,3µm-D-NC-3 over a 24-hour period.

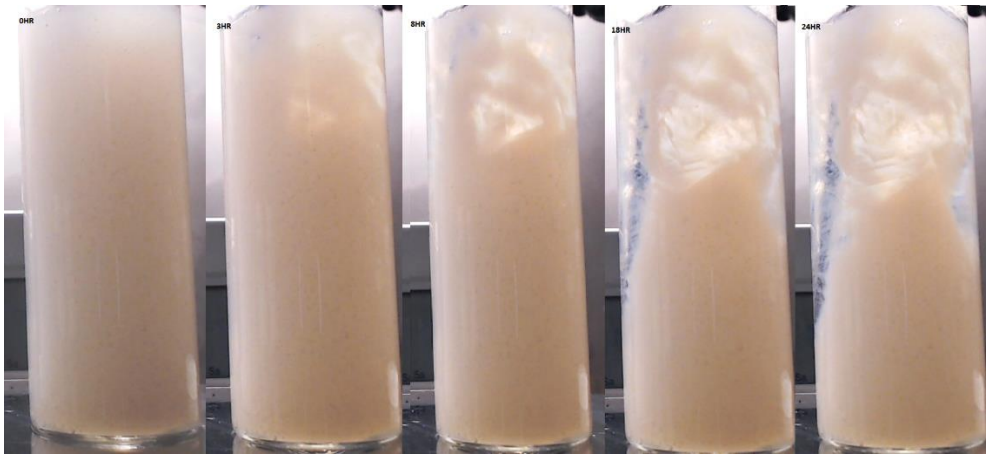

Figure 4-8: Hydrate growth of sample 0,3µm-D-NC-4 over a 24-hour period.

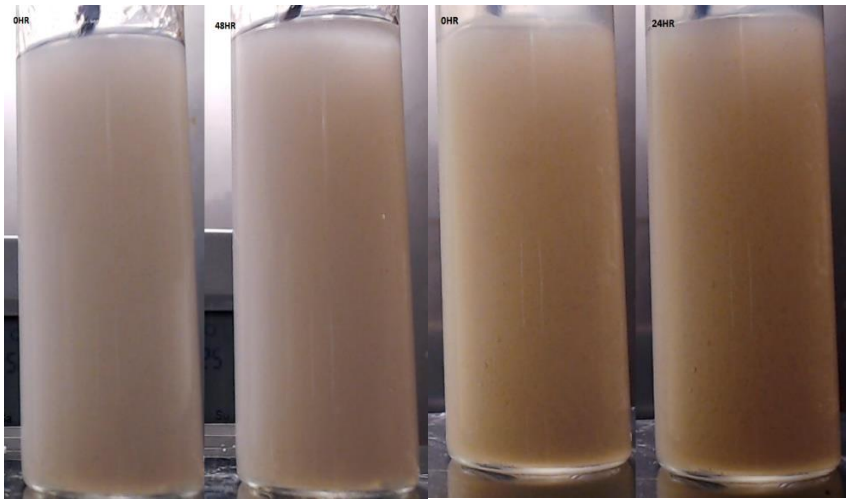

Figure 4-9: Failed hydrate growth in sample 12nm-D-NC-2 (left) and sample 0,3µm-D-NC-5 (right)

Hydrate nucleation was attempted on Sample 12nm-D-NC-2 and 0,3µm-D-NC-5 two times with no luck. It is suggested that local temperature variations in the freezer caused the 0,5g grains of ice to completely melt before a sufficient amount of hydrate was present to sustain hydrate growth.

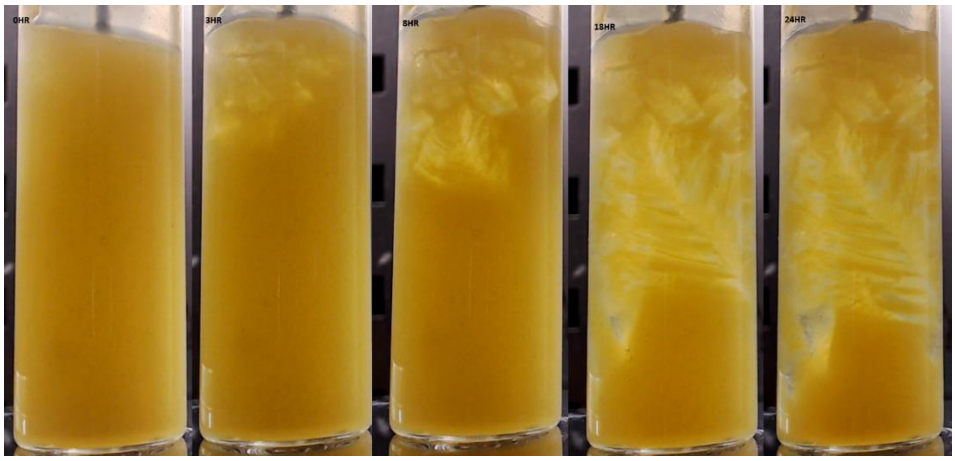

Figure 4-10: Hydrate growth of sample 12nm-D-C-test over a 24-hour period.

Figure 4-10 shows a test sample to observe the effects of adding bromothymol blue as colouring. The sample is yellow as the pH of the THF/water mixture is slightly lower than 6. The colouring does not enter the hydrate crystal structure. As the hydrate crystals grow, the colouring is forced out and concentrated in the remaining solution surrounding the silica particles. As more transparent hydrates appear, the intensity of the colouring becomes stronger, leading to clearly visible boundaries of the displaced silica.

The following run tested the new setup through windows 10´s standard camera software. Six samples were recorded simultaneously by using the time lapse function. This allowed for higher quality pictures.

Figure 4-11: Samples from left to right; 12nm-D-C-1, -2, -3 and 0,3µm-D-C-1, -2, -3. This figure shows the samples three hours after nucleation by ice seeding.

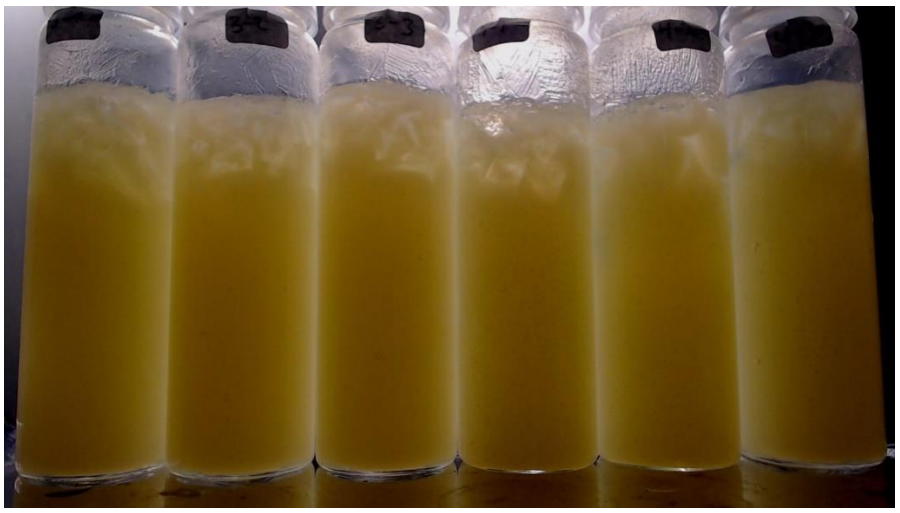

Figure 4-12: Samples from left to right; 12nm-D-C-1, -2, -3 and 0,3µm-D-C-1, -2, -3. This figure shows the samples eight hours after ice seeding.

Figure 4-13: Samples from left to right; 12nm-D-C-1, -2, -3 and 0,3µm-D-C-1, -2, -3. This figure shows the samples 18 hours after ice seeding.

Figure 4-14: Samples from left to right; 12nm-D-C-1, -2, -3 and 0,3µm-D-C-1, -2, -3. This figure shows the samples 24 hours after ice seeding.

4.3 Hydrate growth in varying environmental conditions

Section 4.3 describes the progressive hydrate growth in varying environmental conditions for 0,2-0,3µm silica suspensions and Micro5 sand. Sample series 0,3µm-D-C denotes colloidal silica with a 17:1 mole ratio THF/distilled water solution. Series 0,3µm-3,5%-C denotes the addition of 3,5 weight percent salt, and 0,3µm-U-C denotes samples containing Utsira formation water instead of distilled water. Utsira formation water has an

electrolyte concentration of roughly 3,2 weight percent. Series M5-D-C, M5-3,5%-C and M5-3,5%-U present the same chemical environments with Micro5 sand instead of colloidal silica.

For each of these three sample types, two samples were made with varying amount of liquid content. This was to observe how the porosity affects hydrate growth. In all, six samples were recorded simultaneously. For the Micro5 quartz sand consisting of a silt/clay/sand blend, two parallels of each electrolyte composition were run simultaneously for a total of six samples. The Micro5 sample series is denoted as M5-x-x-x.

Figure 4-15: Samples from left to right; 0,3µm-D-C: -4, -7, 0,3µm-3,5%-C: -1, -4 and 0,3µm-U-C: -1, -4. This figure shows the samples 3 hours after ice seeding.

Figure 4-16: Samples from left to right; 0,3µm-D-C: -4, -7, 0,3µm-3,5%-C: -1, -4 and 0,3µm-U-C: -1, -4. This figure shows the samples 48 hours after ice seeding.

The U- sample series are green due to the pH values of Utsira formation water. Bromothymol blue is yellow at pH values less than 6, green at neutral pH values and blue at basic pH values.

The temperature of the samples in figure 4-15 and 4-16 was supposed to be 0ºC, but due to deviations in the freezer console and the actual temperature, the temperature was roughly 2ºC. This led to hydrate growth in only the saltless samples. This was adjusted in later parallels by setting the temperature on the console to -4ºC. The Freezer cools by supplying cold air with timed breaks. This led to a temperature swing of roughly half a degree. The temperature stabilized at -0,5±0,5ºC, measured in an external container of water and salt. The ice formation above the samples is due to vapor over the samples being more sensitive to the cooling cycles of the freezer. This frosting was also enhanced by the defrosting feature every eight hours. Attempts to turn this feature off were unsuccessful. The samples did not appear to contain ice at the given temperature, as hydrates did not grow before ice was added.

The temperature was monitored in test samples, and as long as hydrates were developed, the defrosting would not lead to dissociation. The defrosting feature turned off the cold air supply for roughly one hour, and no melting was observed in hydrate samples with or without salt. It is therefore assumed that the structures were pure hydrates. Exceptions to this are the samples containing less liquid. These samples had a gel consistency where air was easily trapped. This led to some frost growth, but it was easily differentiated from hydrates.

Figure 4-17 below shows the temperature spike due to the defrosting feature in sample 12nm-D-C-1. The temperature stabilizes as hydrates grow, as solid hydrates act as an insulator.

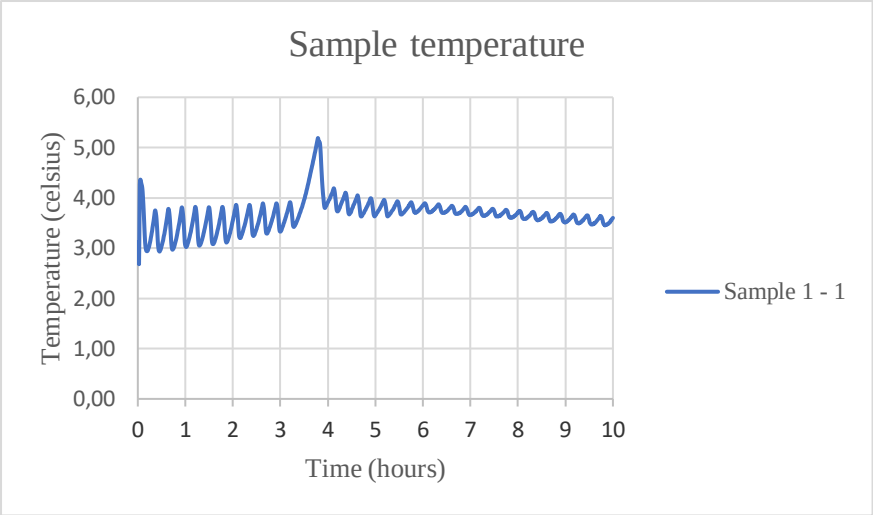

Figure 4-17: Temperature monitoring of sample 1-1 to ensure defrosting does not destroy the hydrates.

For the following parallels, the samples were rearranged into a more straightforwardly manner. Categorizing them by porosity rather than electrolyte composition allows for easier comparison between different environments.

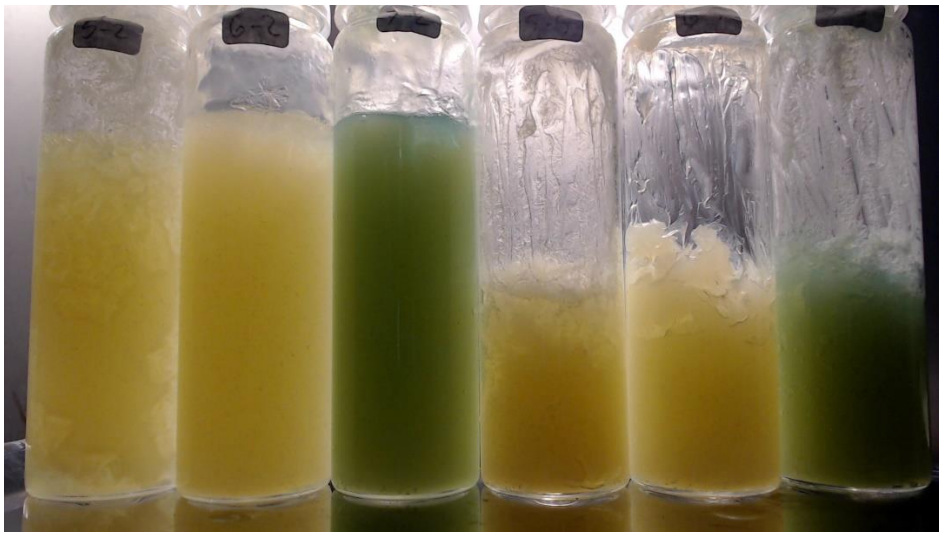

Figure 4-18: 30-minute growth. Samples from left to right: 0,3µm-D-C-5, 0,3µm-3,5%-C-2, 0,3µm-U-C-2, 0,3µm-D-C-8, 0,3µm-3,5%-C-5 and 0,3µm-U-C-5.

Significant hydrate growth is observed in 0,3µm-D-C-5 30 minutes after ice-seeding. After hydrate growth is initiated at the nucleation site, growth is greatly enhanced around the edges of the sample.

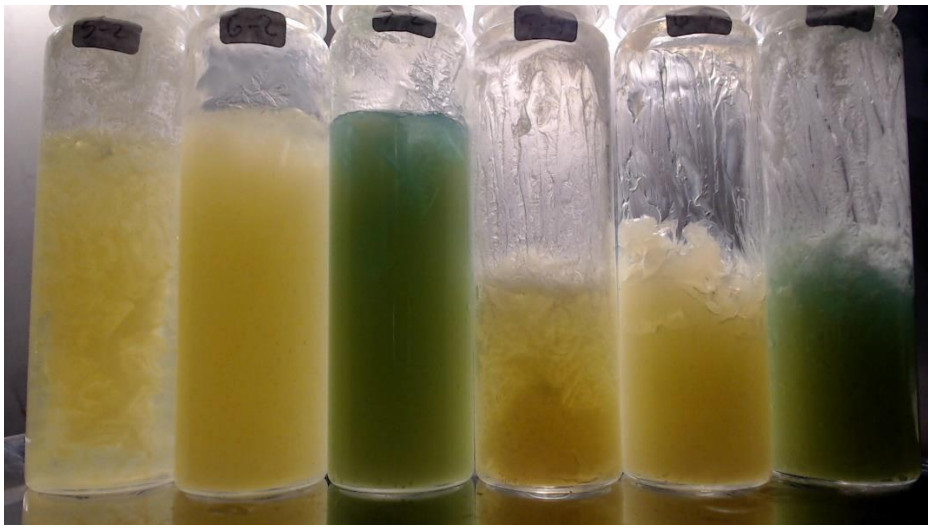

Figure 4-19: 90-minute growth. Samples from left to right: 0,3µm-D-C-5, 0,3µm-3,5%-C-2, 0,3µm-U-C-2, 0,3µm-D-C-8, 0,3µm-3,5%-C-5 and 0,3µm-U-C-5.

Hydrate growth after 90 minutes. The saltless sample 0,3µm-D-C-5 is almost completely crystallized. Sample 0,3µm-U-C-2 is starting to show accelerated growth.

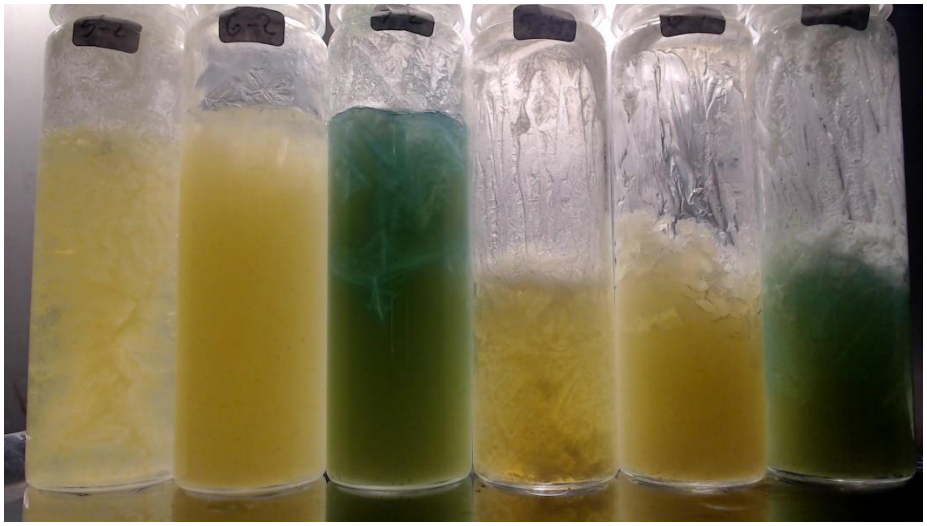

Figure 4-20: 3,5-hour growth. Samples from left to right: 0,3µm-D-C-5, 0,3µm-3,5%-C-2, 0,3µm-U-C-2, 0,3µm-D-C-8, 0,3µm-3,5%-C-5 and 0,3µm-U-C-5.

Hydrate growth after three and a half hours. Sample 0,3µm-D-C-5 and 0,3µm-D-C-8 have completely crystallized. Utsira sample 0,3µm-U-C-2 has started to display significant hydrate growth.

Figure 4-21: 12-hour growth. Samples from left to right: 0,3µm-D-C-5, 0,3µm-3,5%-C-2, 0,3µm-U-C-2, 0,3µm-D-C-8, 0,3µm-3,5%-C-5 and 0,3µm-U-C-5.

Complete hydrate growth in all samples apart from the 3,5wt% NaCl samples 0,3µm-3,5%-2 and 0,3µm-3,5%-5 after 12 hours. Some frost growth is at the bottom of sample 0,3µm-D-C-8.

Figure 4-22: 48-hour growth. Samples from left to right: 0,3µm-D-C-5, 0,3µm-3,5%-C-2, 0,3µm-U-C-2, 0,3µm-D-C-8, 0,3µm-3,5%-C-5 and 0,3µm-U-C-5.

The 3,5wt% NaCl samples see accelerated hydrate growth. A significant amount of frost is observed in sample 0,3µm-3,5%-C-5.

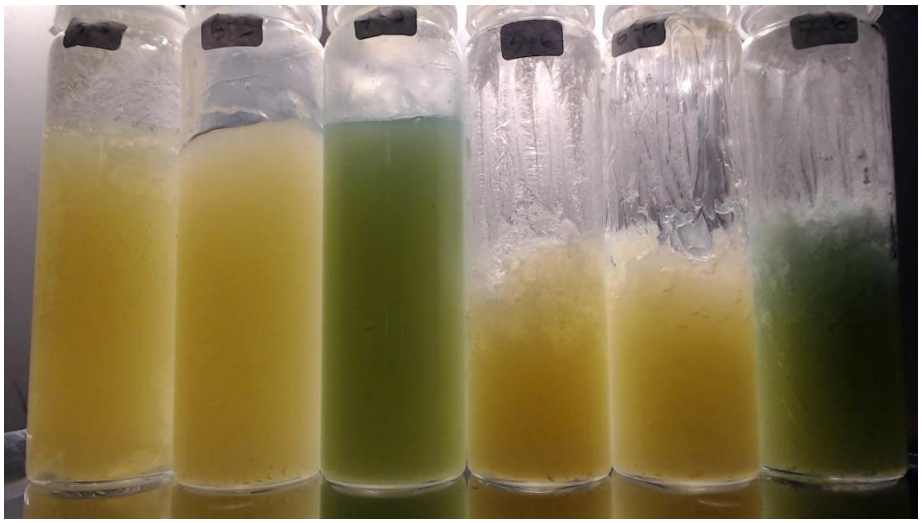

Figure 4-23: 30-minute growth. Samples from left to right: 0,3µm-D-C-6, 0,3µm-3,5%-C-3, 0,3µm-U-C-3, 0,3µm-D-C-9, 0,3µm-3,5%-C-6 and 0,3µm-U-C-6.

Hydrate growth is initiated in saltless samples 0,3µm-D-C-6 and 0,3µm-D-C-9, 30 minutes after ice seeding.

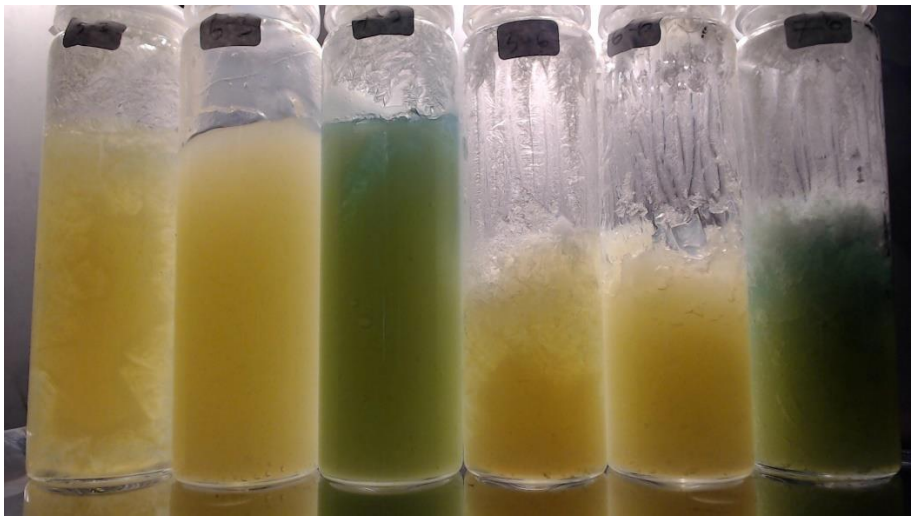

Figure 4-24: 90-minute growth. Samples from left to right: 0,3µm-D-C-6, 0,3µm-3,5%-3, 0,3µm-U-C-3, 0,3µm-D-C-9, 0,3µm-3,5%-6 and 0,3µm-U-C-6.

Hydrate growth is initialized in sample 0,3µm-U-C-3 after 90 minutes. After hydrate growth is initiated at the nucleation site in sample 0,3µm-D-C-6, growth is greatly accelerated around the glass boundary.

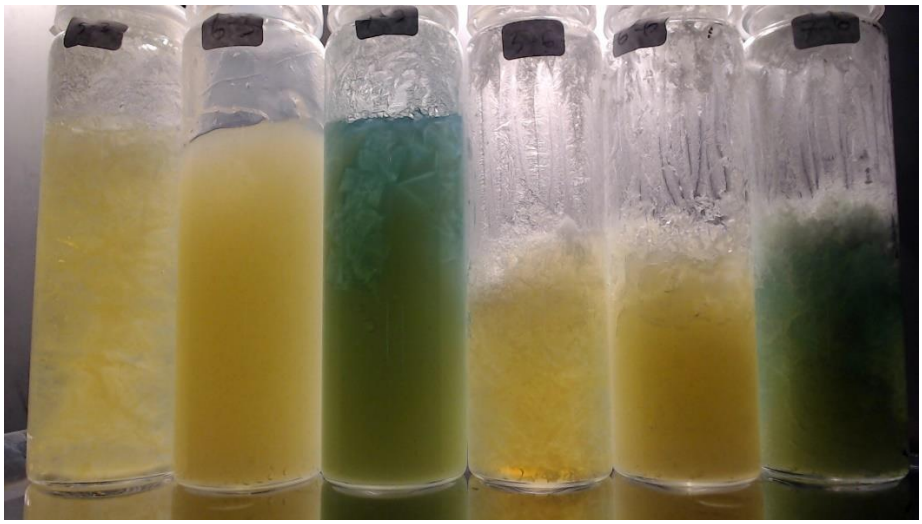

Figure 4-25: 6-hour growth. Samples from left to right: 0,3µm-D-C-6, 0,3µm-3,5%-3, 0,3µm-U-C-3, 0,3µm-D-C-9, 0,3µm-3,5%-6 and 0,3µm-U-C-6.

After six hours, complete hydrate growth in saltless samples 0,3µm-D-C-6 and 0,3µm-D-C-9. Utsira sample 0,3µm-U-C-3 shows significant hydrate growth.

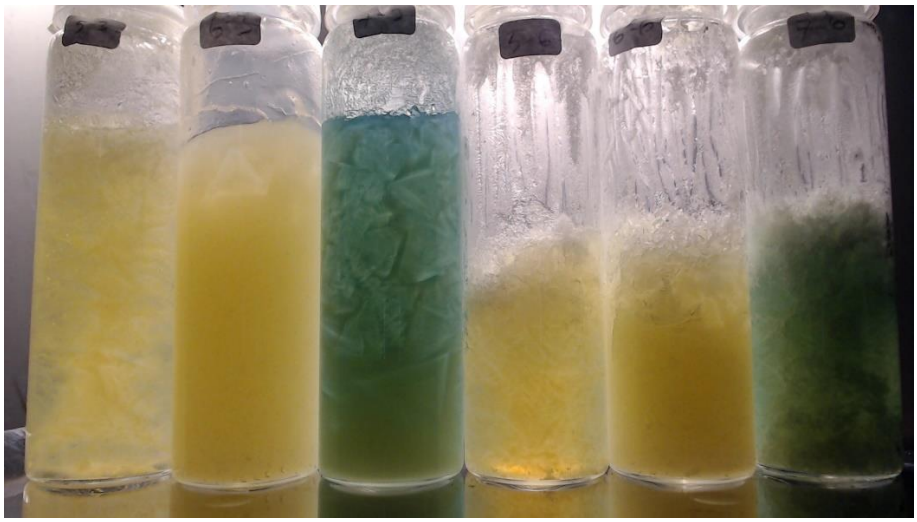

Figure 4-26: 9-hour growth. Samples from left to right: 0,3µm-D-C-6, 0,3µm-3,5%-3, 0,3µm-U-C-3, 0,3µm-D-C-9, 0,3µm-3,5%-6 and 0,3µm-U-C-6.

After nine hours, almost complete hydrate growth is observed in Utsira samples 0,3µm-U-C-3 and 0,3µm-U-C-6. Hydrate nucleation is initiated in 3,5wt% salt samples 0,3µm-3,5%-3 and 0,3µm-3,5%-6.

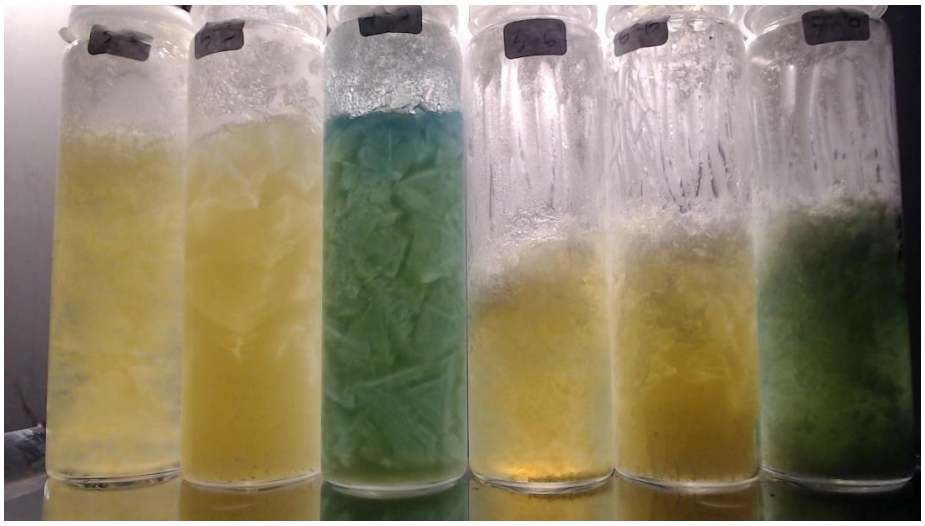

Figure 4-27: 48-hour growth. Samples from left to right: 0,3µm-D-C-6, 0,3µm-3,5%-3, 0,3µm-U-C-3, 0,3µm-D-C-9, 0,3µm-3,5%-6 and 0,3µm-U-C-6.

Figure 4-28: Close up picture of samples 0,3µm-D-C-6, 0,3µm-3,5%-C-3, and 0,3µm-U-C-3 from left to right. Shot at a different angle using a mobile camera.

The following figures 4-29 to 4-31 show the hydrate growth after 48 hours for the six samples of micro5 quartz sand without salt, with salt and with Utsira formation water. The pictures were shot on a mobile camera after being removed from the freezer. The LED lamp was illuminating the back wall to observe the hydrate growth more easily as seen in the previous colloidal samples. As the micro5 quartz sand consolidated into solid white sediment, it allowed no light to pass through. This resulted in low visibility on camera due to the camera

exposure around the samples. The growth over a 48-hour period of these six samples is therefore omitted.

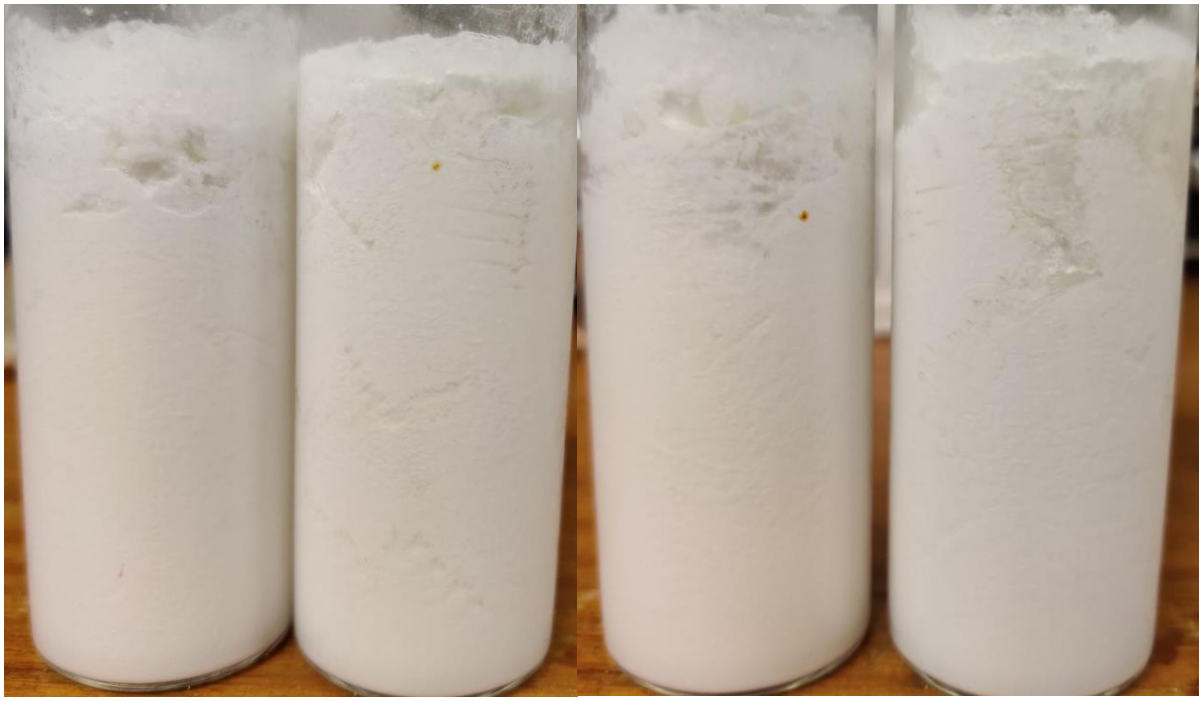

Figure 4-29: M5-D-C-1 and M5-D-C-2 frontside (left) and rear (right) 48 hours after nucleation. The two yellow specks visible are tiny undissolved agglomerates of colouring. Some frost build-up is observed on the glass in the front of sample M5-D-C-1 and the rear of sample M5-D-C-2.

Figure 4-30: M5-3,5%-C-1 and M5-3,5%-C-2 frontside (left) and rear (right) 48 hours after nucleation.

Figure 4-31: M5-U-C-1 and M5-U-C-2 frontside (left) and rear (right) 48 hours after nucleation.

The 3rd and 4th parallels were recorded with the light facing the front of the samples to give better visibility. The vial for sample M5-3,5%-C-4 shattered and was therefore been removed. A small layer of THF/water solution was left above the sediments to allow for easier nucleation.

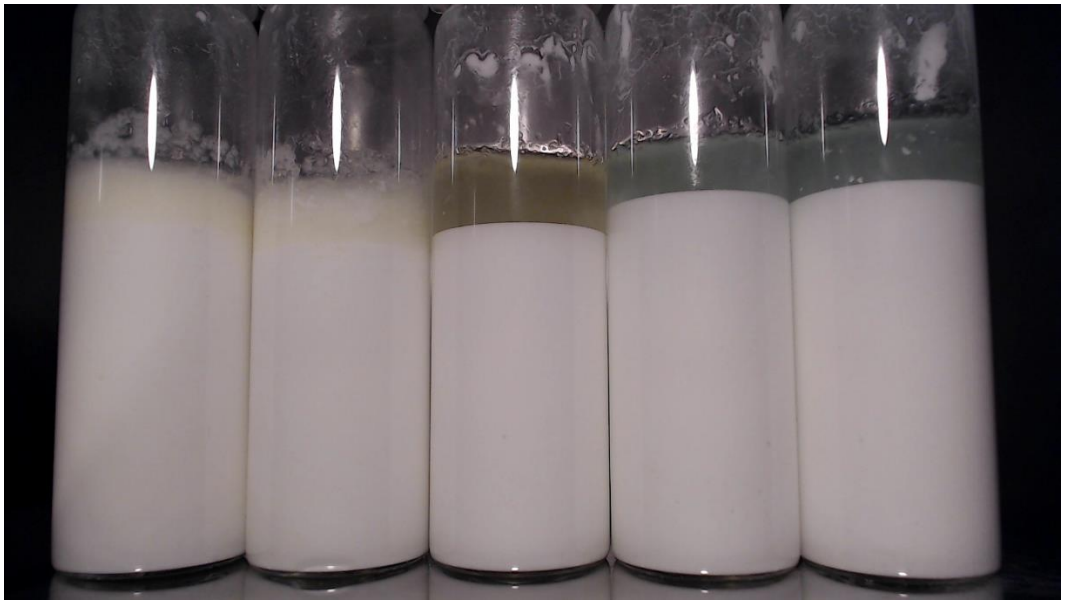

Figure 4-32: Ice seeding at 0 hours. Samples from left to right: M5-D-C-3, -4, M5-3,5%-C-3, M5-U-C-3, -4. The cloudiness of the liquid above sample M5-D-C-3 and M5-D-C-4 stems from the suspension of silt present in Micro5 quartz sand when handling the samples.

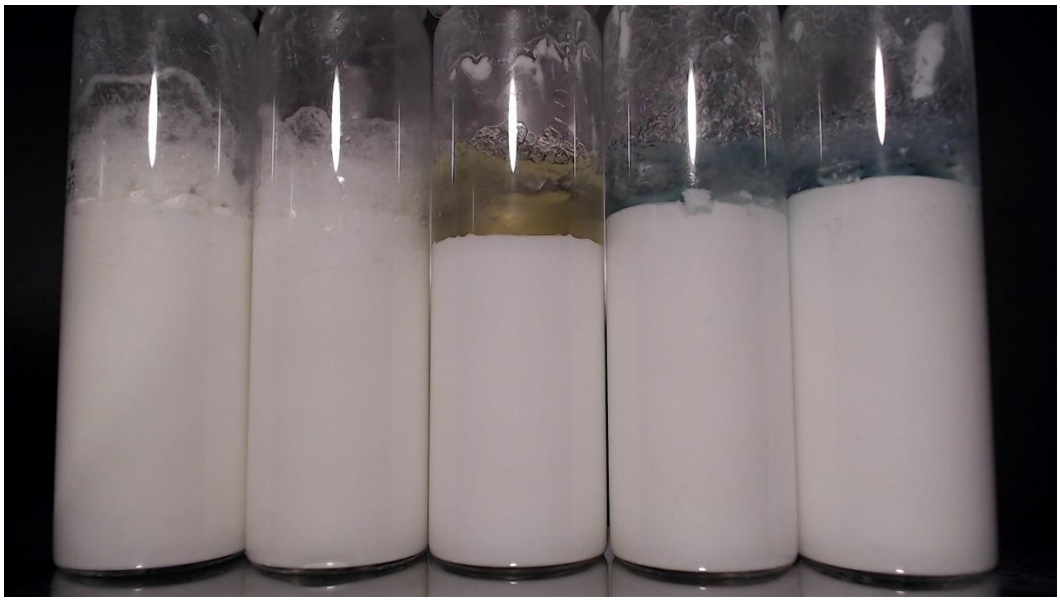

Figure 4-33: 2 hours after nucleation. Samples from left to right: M5-D-C-3, -4, M5-3,5%-C-3, M5-U-C-3, -4.

After two hours, cryo-suction may be observed in all samples apart from M5-3,5%-C-3. Negative fluid pressure pulls liquid into the sediment as hydrates form, and the sediment rises. Some hydrate growth may be observed in these four samples. The sediment in the M5-3,5%-C-3 consolidates slightly.

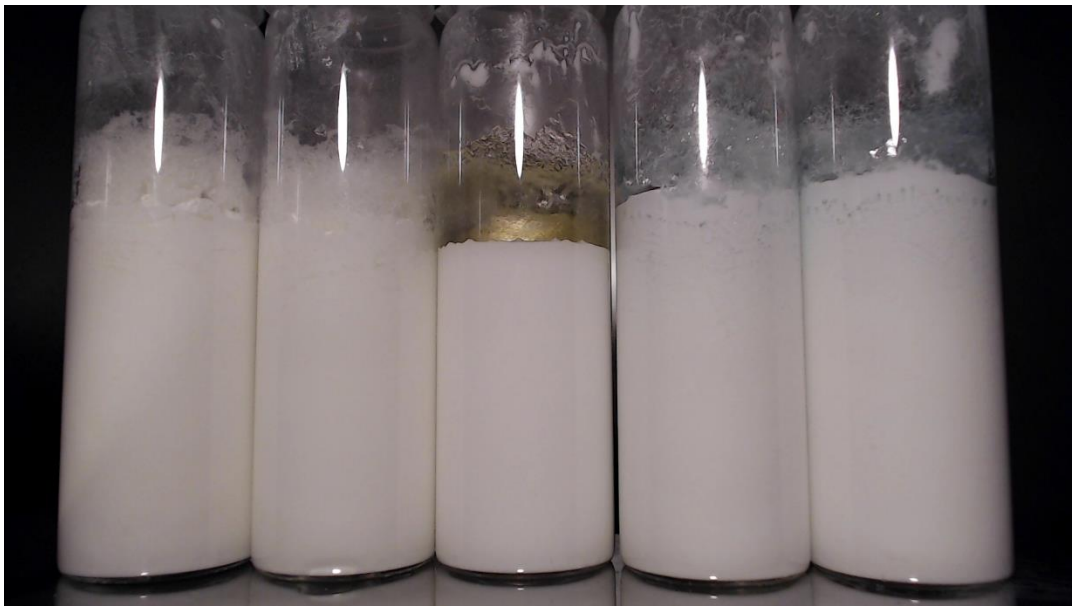

Figure 4-34: 6-hour growth. Samples from left to right: M5-D-C-3, -4, M5-3,5%-C-3, M5-U-C-3, -4.

After six hours, accelerated hydrate growth is observable close to the site of nucleation in all samples apart from M5-3,5%-C-3. The excess liquid solution has begun to enter the sediment in M5-3,5%-C-3 as hydrate nucleation is initiated.

Figure 4-35: 9-hour growth. Samples from left to right: M5-D-C-3, -4, M5-3,5%-C-3, M5-U-C-3, -4.

After nine hours, hydrate growth is also observed in M5-3,5%-C-3. Significant growth is observed in M5-D-C-3, M5-D-C-4, M5-U-C-3, and M5-U-C-4. The green/teal colour of the bromothymol blue in Utsira formation water makes the growth more visible than in the saltless counterparts.

Figure 4-36: 24-hour growth. Samples from left to right: M5-D-C-3, -4, M5-3,5%-C-3, M5-U-C-3, -4.

After 24 hours, significant growth is observed in all samples.

Figure 4-37: Samples from left to right 48 hours after nucleation: M5-D-C-3, -4, M5-3,5%-C-3, M5-U-C-3, -4.

Figure 4-37 shows the rear side of the 3rd and 4th samples 48 hours after nucleation. More hydrate growth is observed compared to the front as seen on camera in figures 4-32 to 4-36. No additional growth was observed after 24 hours on the front side of the samples.

4.4 Observation of hydrate growth via Magnetic Resonance Imaging

Table 4-4: Table of parameters set in Paravision 6.0 before initiating MRI scans for each sample.

Sample code	FOV	Image size	Number of slices	Slice thickness (mm)	TR (ms)	TE (ms)	Averages	RARE factor
MA1	129,82	200x200	17	2,00	2000,00	7,40	30	2
MA2	129,82	200x200	17	2,00	2000,00	7,40	30	2
MRI-M5-D-1	108,76	200x200	19	2,00	2000,00	7,40	30	2
MRI-M5-D-2	108,76	200x200	19	2,00	2000,00	7,40	30	2
MRI-M5-U-1	108,76	200x200	19	2,00	2000,00	7,40	30	2
MRI-M5-U-2	108,76	200x200	19	2,00	2000,00	7,40	30	2

Table 4-4 describes the parameters set in Paravision 6.0 for each MRI scan. By keeping the scan parameters equal, images may be scaled equally in MATLAB. This allows one to compare images from different scans.

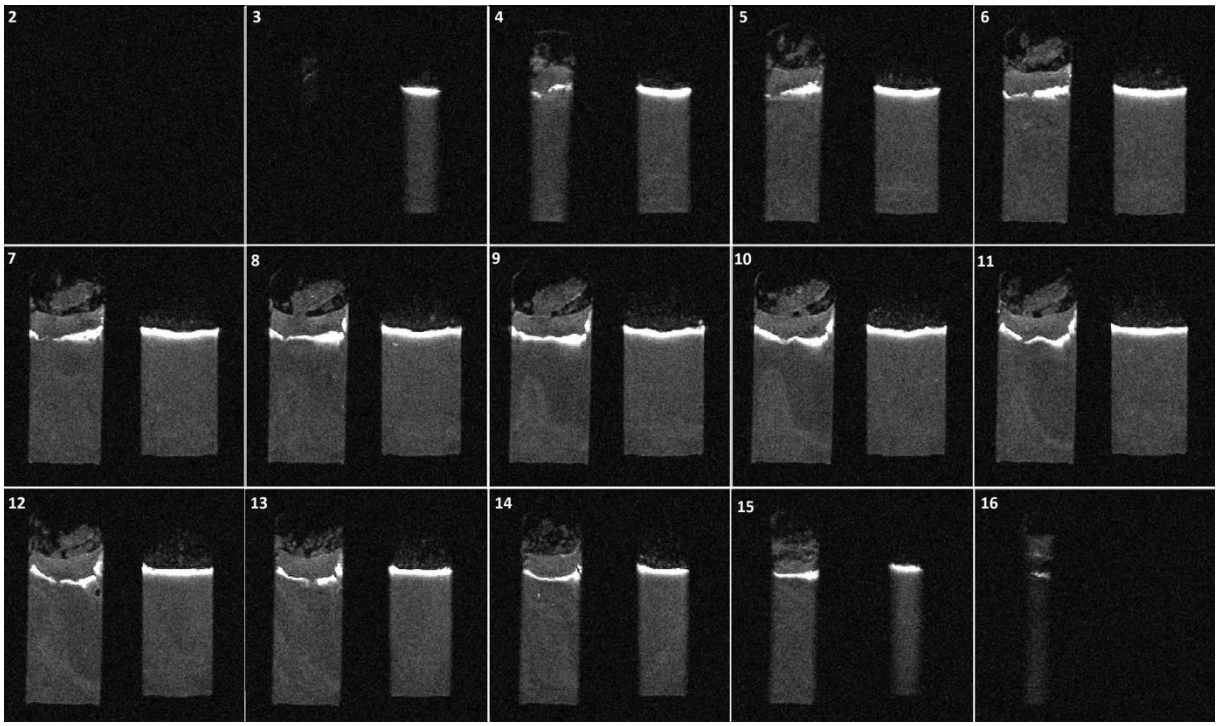

Figure 4-38: MR images of slice 2-16 of sample MA1(left) and MA2(right) taken in the axial plane. The numbering represents the slices from the front of the sample to the rear. These samples were frozen at -18°C for a day before being moved to another freezer set to 3,5°C. White areas indicate areas of high signal intensity, i.e. water and THF solution. Dark areas indicate low signal intensity, i.e. hydrates, ice, air pockets and sand. The grey specks are noise which becomes more apparent as the signal intensity decreases.

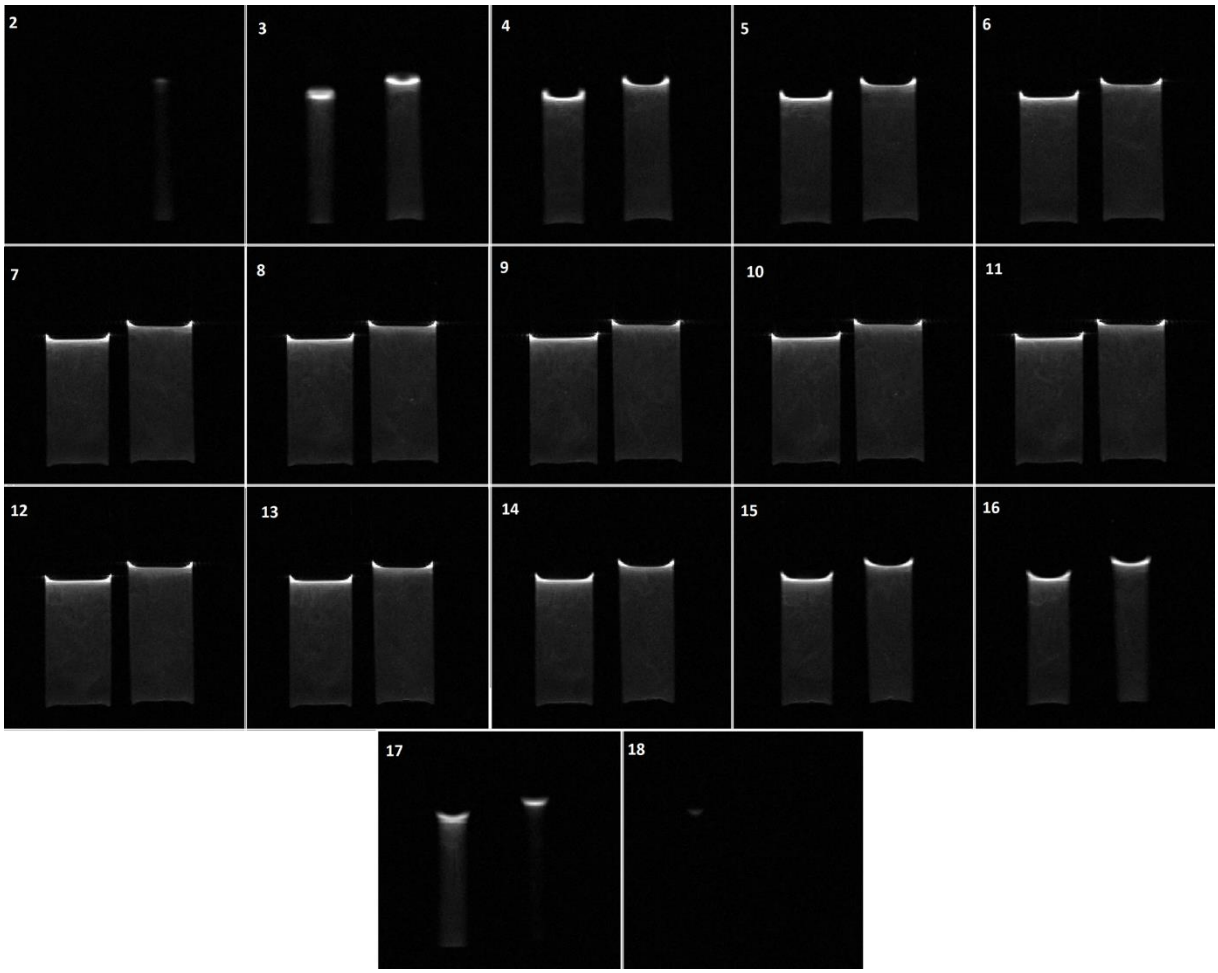

Figure 4-39: MR images of slice 2-18 of sample MRI-M5-D-1 (left) and MRI-M5-D-2 (right) taken in the axial plane. The numbering represents the slices from the front of the sample to the rear. This figure shows the homogenous sediments in the samples after three days of consolidation. The images were taken before hydrate nucleation was initiated via ice-seeding. White areas indicate areas of high signal intensity, i.e. water and THF solution. Dark areas indicate low signal intensity, i.e. air pockets and sand.

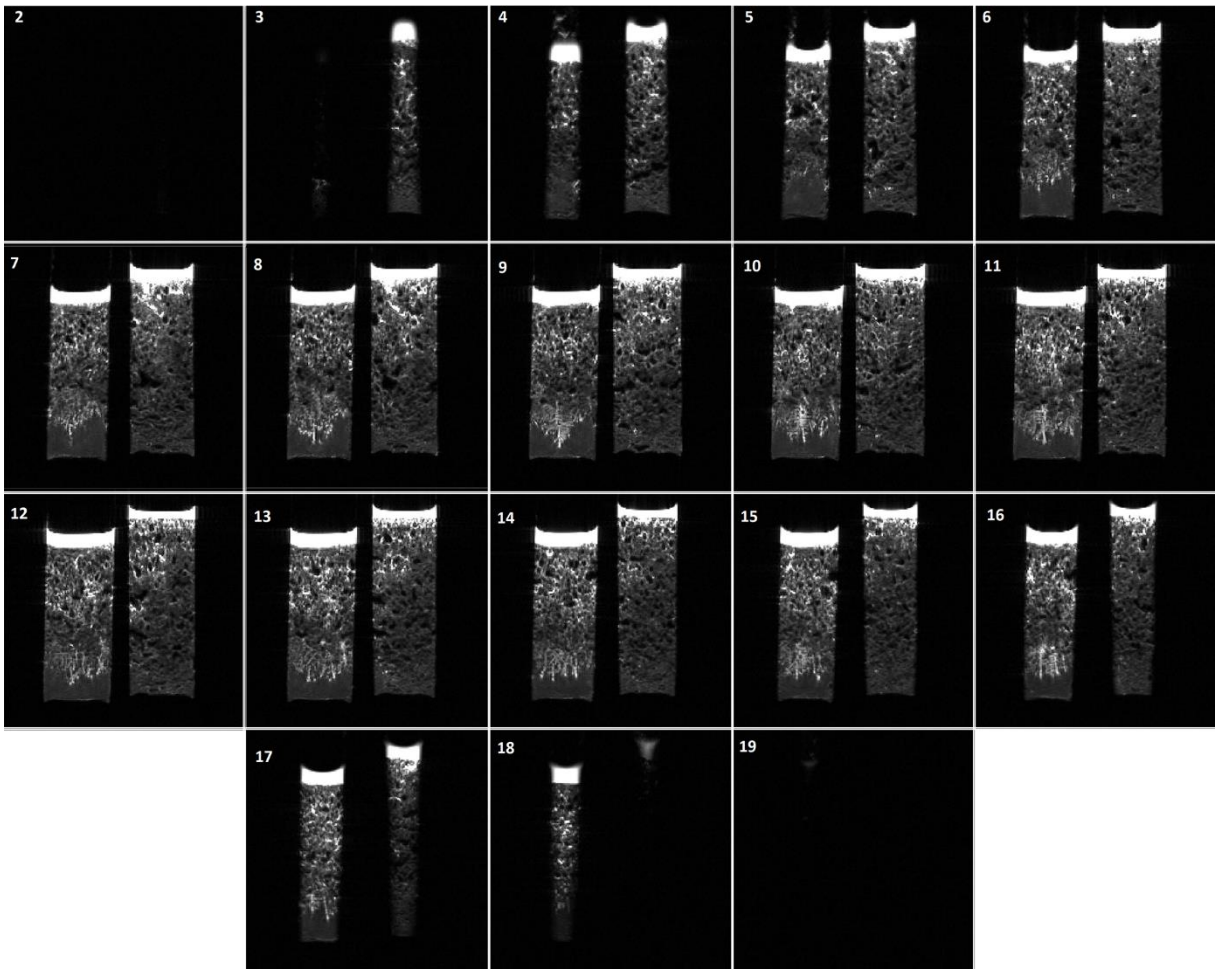

Figure 4-40: MR images of slice 2-19 of sample MRI-M5-U-1 (left) and MRI-M5-U-2 (right) taken in the axial plane. The numbering represents the slices from the front of the sample to the rear. This figure shows the samples after thawing. Hydrate growth was initiated via ice-seeding and the samples were held in a freezer at 0,5°C for 48 hours. White areas indicate areas of high signal intensity, i.e. water and hydrate solution. Dark areas indicate low signal intensity, i.e. hydrates, ice, air pockets and sand.

5 Discussion

The following section discusses the results presented in chapter 4. When viewing electronically as a PDF, one may left click on any figure or sample in the discussion for a hyperlink to the results section for fast viewing. Right click plus “Previous viewing” returns the reader to the discussion.

5.1 Colloidal silica experiments

Figures 4-1 to 4-14 show the growth of 17:1 mole ratio water/THF hydrates in 12nm and 0,2-0,3µm silica suspensions. The site of nucleation was under the surface of the sample. As nucleation is initiated, hydrate crystals grow downwards into the sample from the site of nucleation. The hydrate crystals are identified by the transparent regions in the samples. As the hydrates grow, the white silica is displaced. Through close observation of these samples, it is suggested that there are two dominant growth behaviours of macroscopic hydrate crystals.

Firstly, macroscopic hydrate crystals appear to grow in a triangular formation from the origin of nucleation. Similar growth behaviour is observed for samples of both particle sizes. Samples 12nm-D-NC-4 and 0,3µm-D-NC-4 provide excellent examples of this. Figure 5-1 below shows an upscaled cut-out of these two samples.

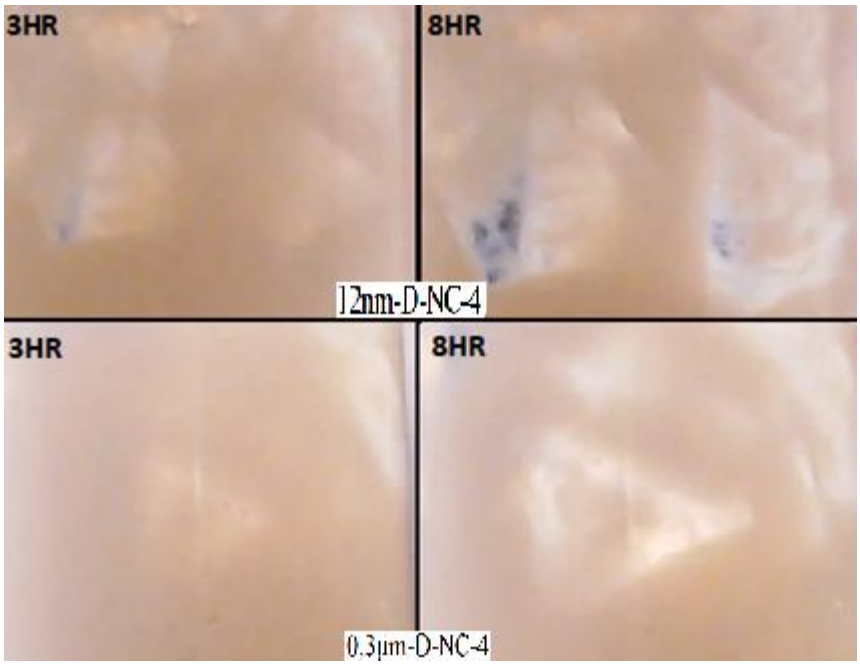

Figure 5-1: Close up of crystal growth in samples 12nm-D-NC-4 and 0,3µm-D-NC-4.

The left images show sample 12nm-D-NC-4 and 0,3µm-D-NC-4 three hours after nucleation and the right image shows them after eight hours. As the THF/water solution is

supplied, the hydrate crystal continuously expands in thin layers around the crystal boundary. As it expands, silica is displaced and trapped in between these layers. This growth behaviour is also easily seen in sample 12nm-D-NC-3 as illustrated in figure 5-2 below.

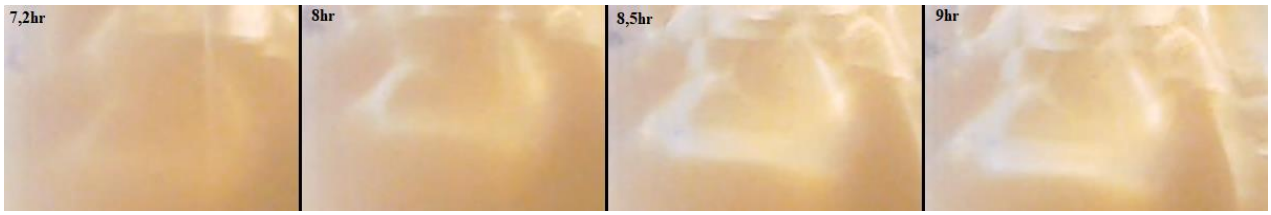

Figure 5-2: Close up of crystal growth in sample 12nm-D-NC-3 after 7,2-9 hours.

After 7,2 hours a triangular crystal periphery becomes visible in the centre of the sample. Shortly after it starts to grow at an accelerated pace. It continuously expands around the edges while displacing silica. The crystal formation appears to develop initially as a shell and expands both inwards and outwards.

Secondly, hydrates are observed to grow veins, sprouting layers as they advance down into the sample. This is best seen in sample 0,3µm-D-NC-2. Figure 5-3 illustrates this behaviour in an upscaled cut-out.

Figure 5-3: Close-up of sample 0,3µm-D-NC-2 24 hours after nucleation. The red arrows highlight where the veins sprout downwards throughout the sample.

Several veins are observed sprouting downwards throughout the sample. The red arrows in figure 5-3 highlight how the veins progress downwards into the sample. As they expand, they branch off into V-shaped layers.

The addition of colouring was also tested to better visualize hydrate growth in the samples. Sample 12nm-D-C-test was added roughly 15ppm of bromothymol blue, which turns yellow at pH values lower than 6. Comparing sample 12nm-D-C-test to the other

samples in figures 4-1 to 4-10 suggests that a colouring concentration of roughly 15 ppm does not affect hydrate growth. Roughly the same amount of hydrates is present after 24 hours for samples with and without colouring. The samples containing colouring also present the same growth patterns. Bromothymol blue was therefore used as a visual indicator in later sets of experiments.

The layering behaviour is also observed in sample 12nm-D-C-test illustrated in figure 4-10 and sample 12nm-D-C-3 in figures 4-12 to 4-14. Figure 5-4 below shows an upscaled cut-out of sample 12nm-D-C-test.

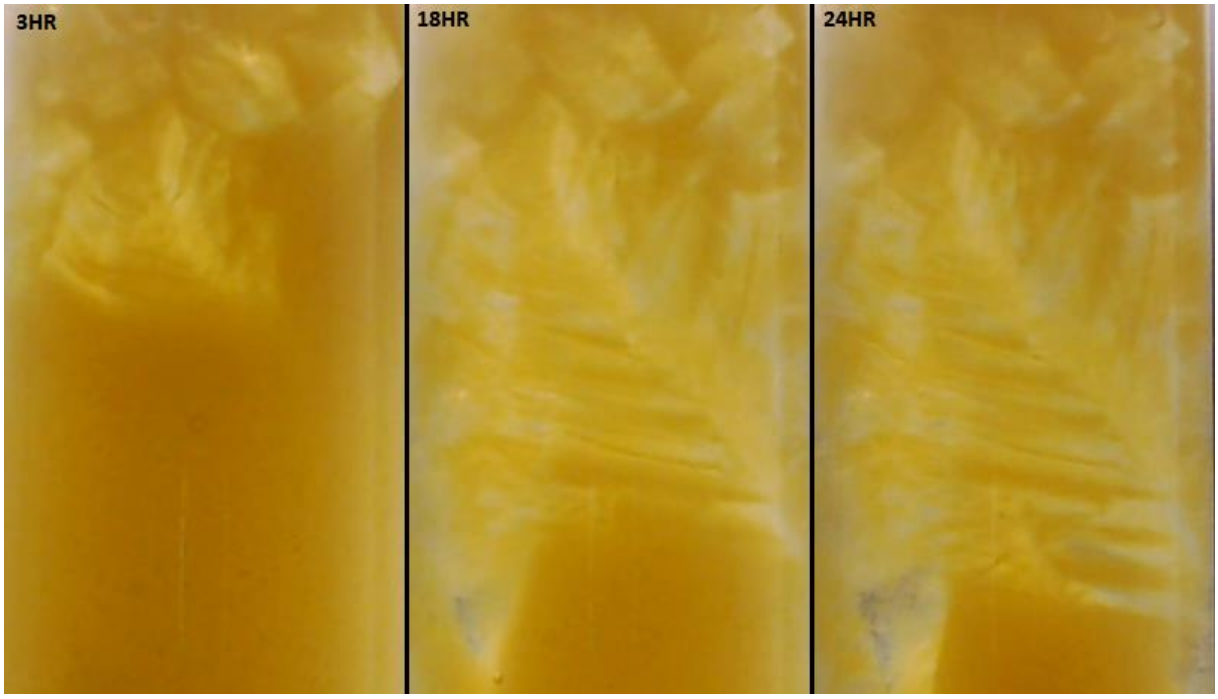

Figure 5-4: Close up of silica layering in sample 12nm-D-C-test.

Comparing the series 12nm-D-NC and 0,3µm-D-NC in figures 4-1 to 4-8, similar hydrate growth and layering is observed. Exceptions to this are samples 12nm-D-NC-3 in figure 4-2, and sample 0,3µm-D-NC-1 in figure 4-5. Sample 12nm-D-NC-3 is the only sample to see complete hydrate growth within 24 hours, while sample 0,3µm-D-NC-1 sees impeded growth.

L.Lei and J.C Santamarina report that capillarity and water-mineral interactions inhibit hydrate growth and shift the phase-equilibrium line to lower temperatures and higher pressures in fine grained sediments (1). Smaller pores cause higher driving forces in fine sediments. At first glance it appears that the 12nm suspensions see faster hydrate growth. There are however some conflicting results. When including the series 12nm-D-C and 0,3µm-

D-C containing colouring, the latter appears to grow hydrates at a faster rate. In the samples without colouring, the temperature sensors are submerged into the samples. This allows for additional nucleation locations. It is apparent that the nucleation is enhanced by the presence of the temperature sensors. This is a rather significant source of error. Figure 4-14 shows hydrate growth where samples are not disturbed by additional nucleation sites. Here the 12nm samples see slower growth rates than the larger 0,2-0,3μm suspensions. It is therefore suggested that L.Lei and J.C Santamarinas' statement also complies with colloidal suspensions, but it is not conclusive. One cannot exclude the uncertainty of the added colouring, but upon close observation it does not appear to have a significant effect on growth rates.

5.2 Environmental conditions experiments

Hydrates were nucleated and grown in three different environments. Sample series denoted by D-C represents 17:1 mole ratio of pure distilled water and THF solution. Sample series denoted by 3,5%-C has the addition of 3,5wt% NaCl, and sample series denoted by U-C contains Utsira formation water with an electrolyte concentration of roughly 3,2wt%. Several samples were prepared with both 0,2-0,3μm colloidal silica and Micro5 quartz sand to test various porosities.

Several successful attempts at hydrate growth by ice-seeding imply a strong relationship between hydrate morphology and sedimentary conditions. It is stated that massive, nodular and veined hydrates occur by stress induced from surrounding sediments and hydrate crystal growth (2). It is observed that the occurrence of these larger hydrate structures also depends on hydrate growth rates.

Faster hydrate nucleation lead to a uniform and disseminated hydrate growth throughout the pore space. This is induced either by low temperatures, higher porosity, or an abundance of nucleation sites. When environmental conditions approach the boundaries of hydrate stability, hydrates accumulate in the form of layers, channels, and nodes. This behaviour is most easily seen in the samples containing electrolytes or lower porosities.

The colloidal silica suspension with a 98% porosity is represented by the samples 4,5 and 6 for the distilled water containing samples, and 1,2 and 3 for the salt and Utsira samples. Sample number 7, 8 and 9 denotes the 96-97% suspension for the distilled water samples, and 4,5 and 6 for the salt and Utsira samples. The 96-97% porosity samples were prepared by

adding half the amount of liquid. The Micro5 samples were prepared with a porosity of roughly 62%. Table 4-2 lists sample properties in complete detail.

The saltless samples 0,3µm-D-C-5, -6, -8 and -9 crystallized at an accelerated rate compared to the 4th and 7th samples due to the temperature being -0,5ºC instead of 2°C. This was to ensure hydrate growth in salt containing samples. Figures 4-18 to 4-28 show how these samples of high growth rates see a uniform dispersal of silica. Sample 0,3µm-D-C-7 in figure 4-15 also contains no electrolytes, but a slow growth rate at 2ºC resulted in larger hydrate channels. Figure 5-5 below compiles together samples 0,3µm-D-C-7, 0,3µm-3,5%-C-2, 0,3µm-3,5%-C-3, 0,3µm-U-C-2, 0,3µm-U-C-3 at 48 hours after nucleation.

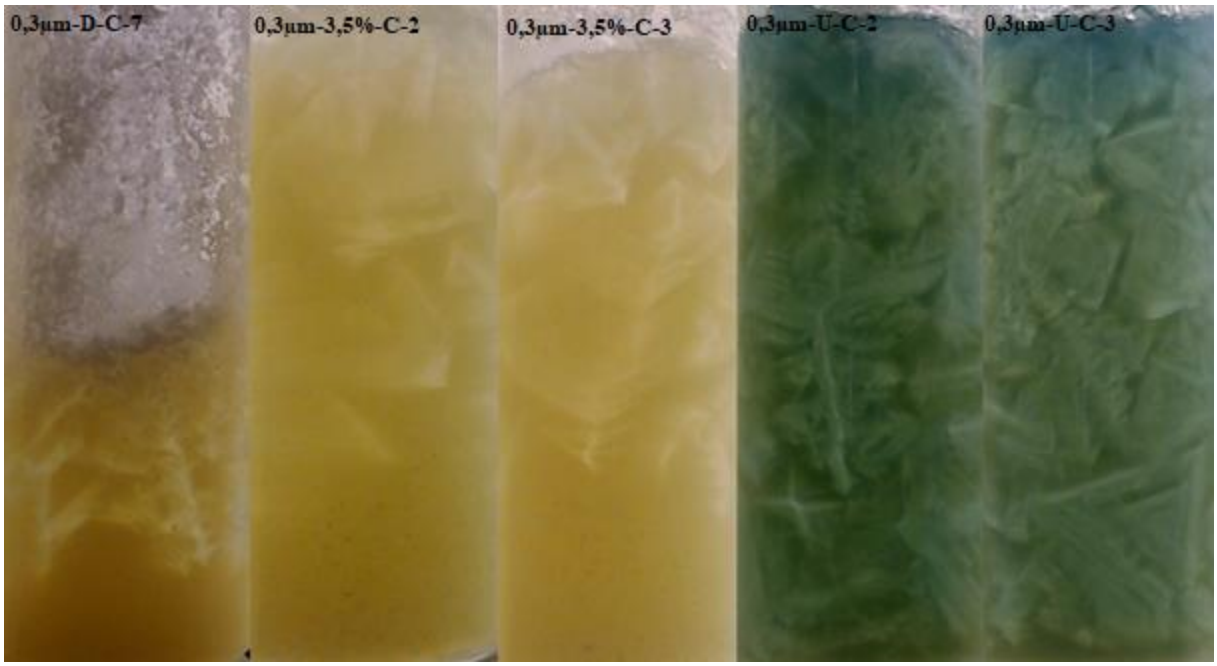

Figure 5-5: Samples from left to right 0,3µm-D-C-7, 0,3µm-3,5%-C-2, 0,3µm-3,5%-C-3, 0,3µm-U-C-2, 0,3µm-U-C-3. This figure shows the larger channels and layers in low hydrate growth rate samples, only 0,3µm-D-C-7 does not contain electrolytes.

Figure 5-5 shows the hydrate growth of sample 0,3µm-D-C-7, 0,3µm-3,5%-C-2, 0,3µm-3,5%-C-3, 0,3µm-U-C-2, 0,3µm-U-C-3 after 48 hours. The deepest channels and layers are observed in the samples 0,3µm-D-C-7, 0,3µm-3,5%-C-2 and 0,3µm-3,5%-C-3, which have the least hydrate growth. One may observe in sample 0,3µm-U-C-2 how a transparent vein advances down into the sample while diffusing silica into layers around it. The triangular crystallization from a nucleation site may also be observed in the Utsira sample 0,3µm-U-C-3.

Figure 4-28 shows an alternative angle of samples 0,3µm-D-C-6, 0,3µm-3,5%-C-3 and 0,3µm-U-C-3 shot with a mobile camera. Here one may see the finer dispersion of silica in sample 0,3µm-D-C-6, which saw a complete hydrate growth in six hours. Deep hydrate veins and nodes are observed in sample 0,3µm-3,5%-C-3 and 0,3µm-U-C-3 which required an additional 42 hours to see hydrate growth as presented by Figure 4-28.

Looking at the 96- and 97% porosity samples, they appear to comply with previous statements. The hydrates in sample 0,3µm-D-C-8 and 0,3µm-D-C-9 grow at an accelerated pace in finer layers in comparison to samples 0,3µm-3,5%-C-5 and 0,3µm-3,5%-C-6 containing 3,5 weight percent NaCl. It is however harder to see in these samples, due to the sample size, air bubbles and frost accumulation.

It is observed that a decrease in porosity leads to larger hydrate crystals and veins. This may be visualized by comparing sample 0,3µm-D-C-4 and 0,3µm-D-C-7. Sample 0,3µm-D-C-7 in figure 4-15 has a porosity of roughly 96% and contains no salt. Larger hydrate channels are observed in this sample compared to 0,3µm-D-C-4 which has a porosity of 98%. These two samples are identical apart from the hydrate/water solution content. As smaller pores inhibit hydrate growth, a slower accumulation of hydrates therefore leads larger crystal structures. Sample 0,3µm-D-C-4 saw complete hydrate formation after 32 hours at a volume 63% larger than the 0,3µm-D-C-7. Even after 48 hours, hydrate growth in the latter was not complete. It is suggested that stronger capillarity displaces more silica in the dense more samples.

Figures 4-29 to 4-37 present hydrate growth in fully saturated micro5 quartz sand with and without salt and Utsira formation water. The porosity of the samples was calculated to be 61-64% after subtracting excess solution displaced out of the sediments. The sand in the samples settled for 24 hours. This however, appeared to not be sufficient. The liquid solution appeared to be forced out of the sediments as it consolidated even a week after the samples were prepared. The porosity of the micro5 samples in table 4-2 are therefore slightly overestimated. The samples for the MRI experiments were produced in the same manner but were allowed to settle for five days before the porosity was calculated. These samples as shown in table 4-3 therefore better represent the porosity of all samples containing micro5 quartz sand.

Hydrate growth was observed in all samples containing micro5 sand. The temperature was also slightly adjusted to attempt to keep the average temperature at 0°C. Figure 4-29

show both the front and rear sides of sample M5-D-C-1 and M5-D-C-2 48 hours after hydrate seeding. It may be observed how hydrate formation also displaces silica in solid sediments with a porosity of roughly 50-60%. This displaced structure persisted after melting as reported by L.Lei and J.C Santamarina (1). An excellent example of the layering behaviour may be observed on the front side of sample M5-D-C-2. A vein sprouts downwards as it branches off into horizontal layers. A few large nodes are also observed in both samples, but it is unclear whether this is frost accumulation or hydrates. Apart from the aforementioned, there is not a significant amount of visible hydrate growth in these two saltless samples. It is suggested that the hydrates disseminate into the pore space. As the sediments are fully saturated, the hydrates become load bearing, cementing the quartz grains together.

Figure 4-30 presents samples with 3,5 weight percent salt in the same manner as the previous samples. The salt content in these samples ensures the absence of ice at a temperature of 0°C. A minor amount of hydrate crystals is observed from the outside of both samples. As ice was seeded through the top, the hydrates visible at the bottom rear side of M5-3,5%-C-1 suggest an internal network of hydrates throughout most of the sample.

Hydrate growth after 48 hours in samples containing Utsira formation water are presented in figure 4-31. These samples see widespread hydrate growth throughout the entire boundary of the vials. The dark green hue of the hydrate crystals stem from the bromothymol blue colouring being green at neutral pH values. With a salt concentration of roughly 3,2 weight percent, one may exclude the presence of ice in the samples. Figure 5-6 below provides a magnified view of both samples.

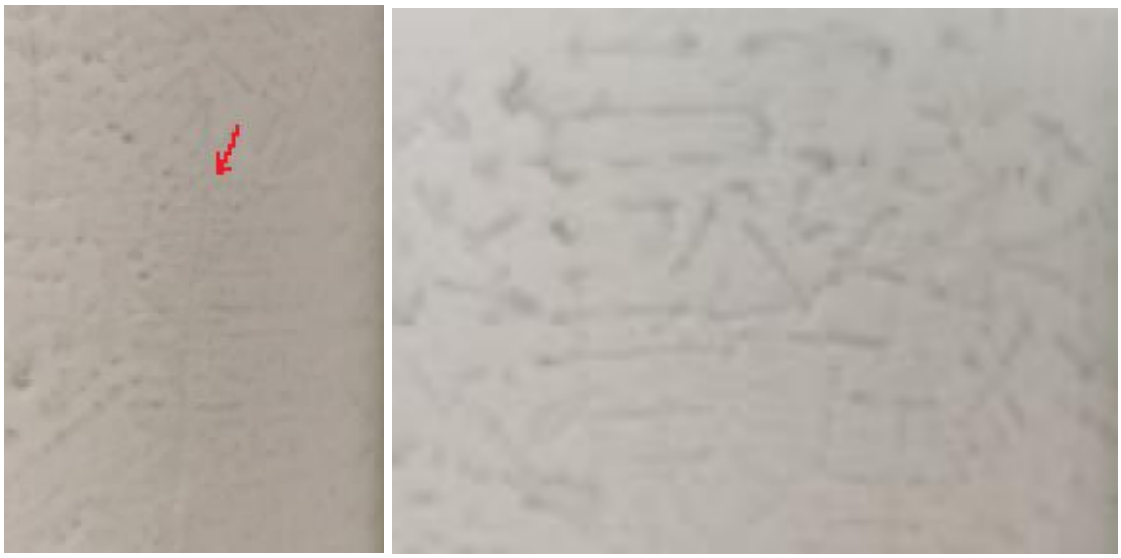

Figure 5-6: Magnified view of hydrate layering in sample M5-U-C-1 (left) and M5-U-C-2 (right). The red arrow shows how a vein sprouts out into horizontal layers as it advances.

The layering behaviour is clearly observed in both these samples. These images serve to confirm that growth behaviours suggested for colloidal suspension also are valid for hydrates in sediments. The red arrow in the left image shows one example of how a vein advances down through sample M5-U-C-1 and branches off horizontally in layers. These horizontal layers are also visible in the right image displaying sample M5-U-C-2. The same triangular crystal nodes are also observed in these samples.

Figure 4-32 to 4-37 present the 3rd and 4th parallels of the Micro5 containing samples. The same observations may be made for these samples. As the ice-seeding is initiated, it may be observed how liquid is forcibly displaced into the sediments before hydrates become visible. This is due to the pressure difference as water molecules are supplied to the hydrate structures. The height of the sand column then expands as the hydrate crystals displaces it. The largest hydrate nodes and veins are observed in these samples containing micro5 sand. The glass vials were extremely fragile and prone to shattering after nucleating hydrates in micro5 sand. This implies that mechanical stress is apparent as hydrates nucleate in these sediments. This complies with the previously stated fact that massive, nodular and veined hydrates occur due to stress induced by hydrate growth (2).

Of the three water environments tested with Micro5 sand, Utsira formation water sees the strongest visible hydrate growth. It is suggested that the natural minerals and sand particles in Utsira formation water act as additional nucleation sites. The least hydrate growth is observed in the samples containing only distilled water and THF. As previously observed in

the colloidal suspensions presented in figure 4-18 to 4-27, the larger hydrate structures do not form in samples of fast hydrate growth. It is suggested that the uniform hydrate structure observed in both 0,3µm-D-C-5 and 0,3µm-D-C-6 is also present in the saltless Micro5 samples.

5.3 Observation of hydrate growth via Magnetic Resonance Imaging

Figure 4-38 to 4-40 presents the results from the MRI experiments performed at Equinor's office at Sandsli. In early March, research was halted due to the ongoing COVID-19 pandemic. This unfortunately left most of the work with the MRI instrument for this thesis cut short. The three experiments presented aimed to lay the groundwork for the methodology with the MRI experiments. This section will therefore discuss the results at hand, and then describe how the approach was to unfold.

The samples were made by adding 17:1 mole ratio pure distilled water and THF to Micro5 quartz sand. Sample MA1 and MA2 employed the strategy of freezing samples to -18 °C over-night, and then moving them to another freezer set to 3,5°C. This was to quickly produce hydrates and ensuring no ice is present in the samples.

Figure 4-38 presents MR image slices of these samples after hydrate dissociation. The images were extracted by using MATLAB and the signal intensity is scaled accordingly so any two images with the same scan parameters may be compared. White indicates areas of high signal intensity, i.e. a high concentration of liquid THF/water. The darker areas represent sand, air pockets or hydrates. The white specks in the background are signal noise. A strip of high signal intensity may be observed at the top of the samples. This is a result of compaction forcing the solution out of the sediments. More sediments were added to the top in an attempt to homogenize it. This was done unsuccessfully, as Micro5 quartz sand tends to cement when in contact with a lesser amount of liquid. For later samples this was avoided by pouring off the top layer of liquid.

The MR images of sample MA1 and MA2 show a homogenous blend of sediments fully saturated in THF solution. It was stated in the previous section how samples with fast growing hydrates do not displace silica in the same manner as samples with slower growth rates. It is suggested that the flash freezing of the samples to -18°C leads to a uniform pore filling hydrate growth. Hydrates therefore do not displace sediments and nucleate into larger structures. Two more experiments were performed with four identical samples to exclude the possibility of a coincidence. These samples yielded the same results and were therefore

omitted. The previously employed strategy where hydrate nucleation was initiated by ice seeding was therefore employed for future experiments.

Figure 4-39 presents sample MRI-M5-D-1 and MRI-M5-D-2 in a pre-scan. This scan was performed to visualize what samples look from within before hydrate growth was initiated. The sand consolidates into a homogenous, fully saturated sediment. These images allow one to compare samples before and after hydrates are grown. Due to the closing of Equinor's office, it was not possible to scan the two aforementioned samples after hydrate growth. Figure 4-40 therefore gives an idea of how samples appear after hydrate growth.

This figure presents MR images of sample MRI-M5-U-1 and MRI-M5-U-2 containing Utsira formation water after dissociation. These samples were prepared in the freezer at the Department of Chemistry at the University of Bergen and brought to Equinor Sandsli. It may be observed how the interior sediment structure has changed after hydrate formation. The areas of high signal intensity represent nodes, channels, and layers of liquid solution where hydrates displaced sediments before dissociation. The black spots are identified as mostly sand and the occasional air pocket. It may be observed how hydrate formation displaces sand and forces it into concentrated areas. Some undisturbed sand may be observed in the bottom of the samples where the hydrates have not yet reached. This is identified by the grey areas of homogenous signal intensity. Slice nine portrays an excellent example of the layering behaviour in hydrates. As the hydrate advances downwards in a channel, it branches off into layers horizontally. Figure 4-40 confirms that layering is prevalent not only at the glass boundaries, but throughout the entirety of the samples.

It was observed that hydrates were dissociated fresh out of the freezer at Equinor. An external temperature logger confirmed the same problem as experienced at the Department of Chemistry. The temperature in the freezer was roughly two degrees warmer than what the freezer console reported.

Fixing this final problem set the methodology for the all the MRI experiments to come. This was unfortunately the moment the pandemic lockdown began, and no more experiments could be performed. The methodology was as follows:

- The samples were to consolidate over a five-day period, and excess solution was to be poured off. This allowed for accurate measurements of the porosity of the samples.

- Hydrates growth was then to be initiated by ice seeding in a water bath set to 0.5°C. This was to ensure a stable temperature, and hydrate growth in samples both with and without salt or Utsira formation water.
- The hydrates were then to be left in the water bath for a period of several days to ensure the presence of a significant amount of hydrates.
- Short MRI scans were to be performed periodically from the moment the samples were removed from the water bath. This was to observe the melting process.
- After dissociation, a longer, higher quality scan would be performed.
- The melting process and post-dissociation images could then be compared with the pre-scan images.

The objective was to study the hydrate layering behaviour inside sediments, and how different chemical environments impacted the hydrate growth. Sample M5-3.5%-C-1 presents an excellent example of how MR imaging is beneficial for studying hydrate growth in sediments. Hydrate growth was initiated from the top of the sample, but only a lesser amount of hydrates was visible from the exterior. As hydrates did not grow before nucleation is initiated, the visible hydrates at the bottom of the sample suggest that an internal network of hydrates is present throughout the sample.

5.4 Hydrate growth behaviour in fine sediments

The transparent nature of colloidal silica suspensions has provided a favourable way to visualize the growth behaviour of THF hydrates. This is further enhanced by the addition of colouring. Hydrates were formed by ice-seeding and were seen to grow via triangular crystallization and veins sprouting into layers. It has been shown that the same growth behaviour is apparent in quartz sediments containing a silt, clay, and sand blend with a porosity of 50-60%. The MRI images provided in figure 4-38 confirm that the layering observed is not a feature bound to the glass contact of the samples.

It is stated that massive, nodular, and veined hydrates occur due to the internal stress in hydrates being larger than the external stress. This is induced by surrounding sediments and hydrate growth (2). Comparing the colloidal silica and micro5 samples, one may observe how larger nodes and veins of hydrate are apparent in the compacted sediments of the latter. As colloidal silica suspensions experience no induced stress, this complies with the statement made above. In the micro5 samples, it was observed how liquid is forced into the sediments by cryo-suction before hydrates became visible. The sediment column then expanded as

hydrates began to grow. This, along with the fact that some vials were prone to shattering after hydrate formation strengthens the theory that an internal stress is present in the samples. Albeit, it may not be proven that this shattering is not a result of sediment compaction.

The growth of nodes, layers, and veins are most prevalent in samples of low hydrate growth rates. This is induced by conditions close to the boundaries of hydrate stability. This is accomplished through temperature adjustments, addition of THIs such as NaCl or reducing the pore volume. When hydrates grow too fast, they appear to disseminate throughout the sediments into a homogenous pore filling structure, as seen in coarser sediments (11). It is suggested that the hydrate growth overwhelms the capillary drive that displaces sediments to allow for larger hydrate structures. The samples containing Utsira formation water saw the most widespread hydrate growth. It is suggested that hydrate growth is enhanced by the additional nucleation sites brought by the presence of natural minerals and electrolytes.

6 Conclusion

The objective of this thesis was to observe hydrate formation behaviour in colloidal silica and fine sediments, both visually with a video camera and by magnetic resonance imaging. Hydrates were observed to form nodes, veins, channels, and layers. The formation behaviour was seen to depend on reaction kinetics. Slow hydrate formation saw the build-up of larger hydrate structures, while fast hydrate growth saw a fine dispersion of hydrates with lesser sediment displacement.

Colloidal suspensions saw a more complete and dispersed hydrate growth, while larger but fewer hydrate structures were observed in the more dense micro5 sediments. No significant changes in hydrate formation behaviour were observed when Bromothymol blue was added. Colouring therefore allows for better visibility. Utsira formation water with an electrolyte content of roughly 3,2 weight percent was also seen to greatly enhance hydrate growth, despite salt's inhibitive properties.

The MR images provide evidence that hydrate layering behaviour is also prevalent within the undisturbed sediments. Figures 4-39 and 4-40 show samples before and after hydrate formation. A network of interconnected channels, layers and veins is apparent throughout the entirety of the samples. It is possible to observe how hydrate formation has displaced sand and forced it into concentrated areas. The structures persist after hydrate dissociation.

7 Recommendations for further work

As the MRI experiments for this thesis were cut short due to the ongoing COVID-19 pandemic, it is suggested that the layering behaviour of hydrates is more closely examined with RAREst scans in an MRI instrument.

The quartz sand used in this thesis possesses interesting compaction properties when fully saturated in a fluid. Compaction was observed a week after preparation. It is therefore suggested that the quartz sediment should be allowed to consolidate further to exclude uncertainties tied to the migration of fluids out of the sediments. Controlling excess fluid improves the MRI signal considerably. To cut the consolidation time, excitation via vibration may be useful.

In this thesis the THF hydrates were found to form the largest structures when hydrates formed at a slow rate near the phase boundary of hydrate stability. It is recommended that hydrates are grown over a longer time period in order to ensure maximum hydrate growth. Nucleation via ice-seeding in a controlled environment such as a water bath ensures the stability of the hydrates. As THF hydrate growth is significantly enhanced by the Utsira formation water, it would be interesting to investigate the differences between such hydrates and hydrates made with distilled water in an MRI instrument. As external stress affect hydrate growth behaviour, it would be interesting to explore the effects of an overburden pressure. This may be achieved by adding weight over the samples.

List of references

1. L. Lei, J.C. Santamarina. Laboratory Strategies for Hydrate Formationin Fine-Grained Sediments. *Journal of Geophysical Research: Solid Earth.* 2018, ss. 2583-2596.

2. D. Long, M.A. Lovell et. al. *Sediment-hosted gas hydrates: new insights on natural and synthetic systems.* s.l. : Geological Society, London, Special Publications, 319, 1-9, 2009.

3. B. Lal, O. Nashed. *Chemical Additives for Gas Hydrates.* 1st ed. s.l. : Springer International Publishing, 2020. s. 1.

4. Offshore Engineering. [Internett] 2020. https://www.offshoreengineering.com/pipelines/flow-assurance-222/118-pipelines/flow-assurance/156-hydrates [24.03.20].

5. Milkov, A.V. Global estimates of hydrate-bound gas in marine sediments: how much is really out there? *Earth-science reviews.* 66, 2004, 3-4, ss. 183-197.

6. J.Lee, J.W. Kenney III. *Clathrate Hydrates.* s.l. : InTechOpen, 2018. ss. 129-145.

7. C. D. Ruppel, J. D Kessler. The interaction of climate change and methane hydrates. *Review of Geophysics.* 2017, ss. 126-131.

8. Kvenvolden, K. A. Gas Hydrates- Geological Perspective and Global Change. *Review of Geophysics.* 1993, ss. 173-175.

9. GRID-Arendal. GRIDA. *Stability Conditions for Gas Hydrates.* [Internett] 2009. https://www.grida.no/resources/6625 [26.03.20].

10. Z. Zhang, Y. Wang, Lian-Feng Gao et. al. Marine Gas Hydrates: Future Energy or Environmental Killer? *2012 International Conference on Future Energy, Environment, and Materials.* 2012, Energy Procedia 16, ss. 933-938.

11. W. Waite, J.C. Santamarina, D.D. Cortes et al. Physical properties of hydrate-bearing sediments. *Review of Geophysics; Washington.* 47, 4, 2009, ss. 1-38.

12. N. J. English, M. D. MacElroy. Perspectives on molecular simulation of clathrate hydrates: Progress, prospects and challenges. *Chemical Engineering Science.* 2015, 121, ss. 133-156.

13. E. D. Sloan, C. A. Koh. *Clathrate Hydrates of Natural Gases.* 3. 2008. ss. 54-55, 113-115.

14. J.Y. Lee, T.S. Yun, J. C. Santamarina, C. Ruppel. Observations related to tetrahydrofuran and methane hydrates for laboratory studies of hydrate-bearing sediments. *Geochemistry, Geophysics, Geosystems.* 2007.

15. Sigmaaldrich. [Internett] 2020. https://www.sigmaaldrich.com/chemistry/solvents/tetrahydrofuran-center.html [26.03.20].

16. P.W. Wilson, D. Lester, A. D. J. Haymet. Heterogeneous nucleation of clathrates from supercooled tetrahydrofuran (THF)/water mixtures, and the effects of an added catalyst. *Chemical Engineering Science.* 2005, 60, 11, ss. 2937-2941.

17. B. Lal, O. Nashed. *Chemical Additives for Gas Hydrates.* s.l. : Springer International Publishing, Cham, 2020. ss. 27-33.

18. Sabil, K. M. Phase Behaviour, Thermodynamics and Kinetics of Clathrate Hydrate Systems of Carbon Dioxide in Presence of Tetrahydrofuran and Electrolytes. 2009, s. 91.

19. B. A. Baldwin, A. Moradi-Araghi, J. C. Stevens. Monitoring hydrate formation and dissociation in sandstone and bulkwith magnetic resonance imaging. *Magnetic Resonance Imaging.* 2003, 21, ss. 1061-1069.

20. M. Yang, Z. R. Chong, J. Zheng et, al. Advances in nuclear magnetic resonance (NMR) techniques for the investigation of clathrate hydrates. *Renewable and Sustainable Energy Reviews.* 2017, 74, ss. 1346-1360.

21. M. Yang, Y. Song, Y. Zhao et, al. MRI measurements of CO2 hydrate dissociation rate in a porous medium. *Magnetic Resonance Imaging.* 2011, 29, 7, ss. 1007-1013.

22. Heidenreich, M. *System manual for Avance III HD/MRI instruments 1st edition.* s.l. : Bruker Corporation, 2014.

23. Bruker Biospec. [Internett] 2020. https://www.bruker.com/products/mr/preclinical-mri/biospec.html [04.04.20].

24. Singapore Sports and Orthopaedic Clinic. [Internett] 2020. http://www.chanorthopaedics.com.sg/our-services/magnetic-resonance-imaging-mri [04.04.20].

25. Blink, E. J. *Basic MRI physics.* 2004. ss. 1-75.

26. Tetli, E. S. *Application of MRI in studies of tetrahydrofuran hydrates in quartz sand at atmospheric pressure.* s.l. : Department of Chemistry - University of Bergen, 2017. s. 9.

27. A. D. Elster, J. H. Burdette. *Questions and answers in Magnetic Resonance Imaging.* 2. 2001.

28. Johannesen, M. *Clathrate hydrate formation in different chemical environments relevant to subsurface CO2 storage.* s.l. : Department of Chemistry, University of Bergen, 2018. pp. 26-27.

29. *Detection and quantification of Utsira formation water in production wells of the Oseberg Sør Field and impact on scale management.* R. McCartney, E. Moldrheim, N.Fleming. Geilo : s.n., 2010. 21st International Oil Field Chemistry Symposium. p. 11.

30. *Observations related to tetrahydrofuran and methane hydrates for laboratory studies of hydrate-bearing sediments.* J.Y. Lee, T.S. Yun, J. C. Santamarina, C. Ruppel. s.l. : Geochemistry, Geophysics, Geosystems., 2007.

31. Warwick Faculty of Science, Engineering and Medicine. Integrated Magnetic Resonance Centre for Doctoral Training. [Internett] https://warwick.ac.uk/fac/sci/physics/research/condensedmatt/imr_cdt/students/peter_james_ross/rapidimaging/rare/ [01.05.20].

32. A. D. Elster, J. H. Burdette. TR and TE - Questions and answers in Magnetic Resonance Imaging. [Internett] 2001. http://mriquestions.com/tr-and-te.html [04.05.20].

33. D.J. Bell, J. Yeung et al. Radiopaedia. Echotime. [Internett] https://radiopaedia.org/articles/echo-time [01.05.20].

Appendix

Uncertainty estimations

The uncertainties in the equipment used to prepare samples is as shown in the following table:

Table A-1: Table of uncertainties for the equipment used for sample preparation

Instrument	Parameter	Uncertainty
Kern EG420-3NM	Weight	0,01g
PT-100 sensor	Temperature	0,3°C
Testo 176-T4	Temperature	0,1°C
25ml syringe	Volume	0,1ml

Figure A-2 shows the temperature swings observed in the freezer where samples were stored. A swing of roughly ±1°C was observed pre-hydrate formation, which levelled off in the range of °0,5C after formation. Solid hydrates act as an insulator. The big spike in temperature was due to the defrosting sequence in the freezer.

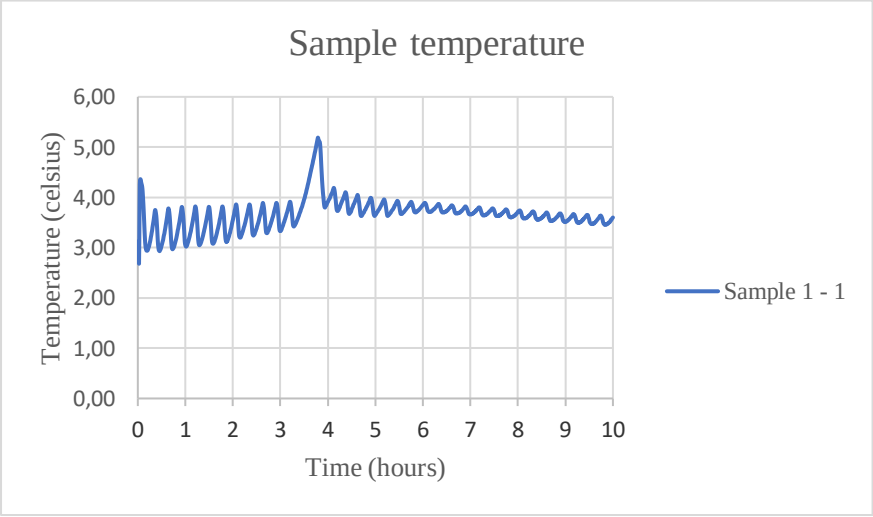

Figure A-2: Temperature monitoring of sample 1-1 showing the temperature swing in samples in the Mastercella Carel Freezer.

Calculations

Molar ratio of 17:1 THF/water solutions were calculated using the following formula:

- $molar\ ratio = \frac{n_1}{n_1+n_2}$, where $n = \frac{m}{m_x}$ **(F.2)**

Where *n* is mole, *m* is mass and m_x is molar weight.

Fluid density in THF/water solutions containing electrolytes was calculated using the following formula:

- $\rho = \frac{V}{m}$ **(F.3)**

Where ρ is the density, v is the liquid volume, and m is the mass of the liquid bulk.

The porosity of sediments was calculated accordingly:

- $ø = \frac{V_{pore}}{V_{bulk}} = \frac{V_{pore}}{V_{matrix}+V_{pore}}$ **(F.4)**

Where *ø* is the porosity, V_p is the pore volume, V_b is the bulk volume, V_{matrix} is the sediment matrix volume.